



**NAVAL
POSTGRADUATE
SCHOOL**

MONTEREY, CALIFORNIA

THESIS

**DESIGN AND ANALYSIS OF MEGAWATT CLASS FREE
ELECTRON LASER WEAPONS**

by

Weisheng Joseph Ng

December 2015

Thesis Advisor:
Co-Advisor:

Joseph Blau
Keith Cohn

Approved for public release; distribution is unlimited

THIS PAGE INTENTIONALLY LEFT BLANK

REPORT DOCUMENTATION PAGE			Form Approved OMB No. 0704-0188
<p>Public reporting burden for this collection of information is estimated to average 1 hour per response, including the time for reviewing instruction, searching existing data sources, gathering and maintaining the data needed, and completing and reviewing the collection of information. Send comments regarding this burden estimate or any other aspect of this collection of information, including suggestions for reducing this burden, to Washington headquarters Services, Directorate for Information Operations and Reports, 1215 Jefferson Davis Highway, Suite 1204, Arlington, VA 22202-4302, and to the Office of Management and Budget, Paperwork Reduction Project (0704-0188) Washington, DC 20503.</p>			
1. AGENCY USE ONLY (Leave blank)	2. REPORT DATE December 2015	3. REPORT TYPE AND DATES COVERED Master's thesis	
4. TITLE AND SUBTITLE DESIGN AND ANALYSIS OF MEGAWATT CLASS FREE ELECTRON LASER WEAPONS		5. FUNDING NUMBERS	
6. AUTHOR(S) Weisheng Joseph Ng			
7. PERFORMING ORGANIZATION NAME(S) AND ADDRESS(ES) Naval Postgraduate School Monterey, CA 93943-5000		8. PERFORMING ORGANIZATION REPORT NUMBER	
9. SPONSORING /MONITORING AGENCY NAME(S) AND ADDRESS(ES) N/A		10. SPONSORING / MONITORING AGENCY REPORT NUMBER	
11. SUPPLEMENTARY NOTES The views expressed in this thesis are those of the author and do not reflect the official policy or position of the Department of Defense or the U.S. Government. IRB Protocol number <u>N/A</u> .			
12a. DISTRIBUTION / AVAILABILITY STATEMENT Approved for public release; distribution is unlimited	12b. DISTRIBUTION CODE A		
13. ABSTRACT (maximum 200 words) <p>Free Electron Lasers (FELs) are desirable for defense against a spectrum of threats, especially in the maritime domain, due to their all-electric nature, their wavelength tunability to atmospheric propagation “sweet-spots,” and their scalability to megawatt class lasers. In this thesis, we exploit these characteristics to design, simulate, and analyze both amplifier and oscillator FELs using the FEL 4-D code developed by the Physics Directed Energy (DE) Group at the Naval Postgraduate School (NPS). Propagation analysis is performed on the designs using the Atmospheric NPS Code for High Energy Laser Optical Propagation (ANCHOR), also developed by the NPS Physics DE Group, to arrive at various lethality estimates that allow us to quantify the weapon’s effectiveness in its operating domain. We conclude that megawatt class FELs, while lacking in technological maturity, would provide an effective defense, especially against hardened, time-critical threats such as sub-sonic and super-sonic anti-ship missiles.</p>			
14. SUBJECT TERMS directed energy weapons, high energy lasers, Free Electron Laser, FEL oscillator, FEL amplifier, FEL modeling, atmospheric propagation modeling			15. NUMBER OF PAGES 93
16. PRICE CODE			
17. SECURITY CLASSIFICATION OF REPORT Unclassified	18. SECURITY CLASSIFICATION OF THIS PAGE Unclassified	19. SECURITY CLASSIFICATION OF ABSTRACT Unclassified	20. LIMITATION OF ABSTRACT UU

THIS PAGE INTENTIONALLY LEFT BLANK

Approved for public release; distribution is unlimited

**DESIGN AND ANALYSIS OF MEGAWATT CLASS FREE ELECTRON LASER
WEAPONS**

Weisheng Joseph Ng
Civilian, Singapore
B.Eng., National University of Singapore, 2004

Submitted in partial fulfillment of the
requirements for the degree of

MASTER OF SCIENCE IN APPLIED PHYSICS

from the

**NAVAL POSTGRADUATE SCHOOL
December 2015**

Approved by: Joseph Blau
 Thesis Advisor

Keith Cohn
Co-Advisor

Kevin Smith
Chair, Department of Physics

THIS PAGE INTENTIONALLY LEFT BLANK

ABSTRACT

Free Electron Lasers (FELs) are desirable for defense against a spectrum of threats, especially in the maritime domain, due to their all-electric nature, their wavelength tunability to atmospheric propagation “sweet-spots,” and their scalability to megawatt class lasers. In this thesis, we exploit these characteristics to design, simulate, and analyze both amplifier and oscillator FELs using the FEL 4-D code developed by the Physics Directed Energy (DE) Group at the Naval Postgraduate School (NPS). Propagation analysis is performed on the designs using the Atmospheric NPS Code for High Energy Laser Optical Propagation (ANCHOR), also developed by the NPS Physics DE Group, to arrive at various lethality estimates that allow us to quantify the weapon’s effectiveness in its operating domain. We conclude that megawatt class FELs, while lacking in technological maturity, would provide an effective defense, especially against hardened, time-critical threats such as sub-sonic and super-sonic anti-ship missiles.

THIS PAGE INTENTIONALLY LEFT BLANK

TABLE OF CONTENTS

I.	INTRODUCTION.....	1
II.	OVERVIEW OF FREE ELECTRON LASERS.....	3
A.	CATHODE	4
B.	INJECTOR.....	4
C.	LINEAR ACCELERATOR.....	5
D.	UNDULATOR AND OPTICS	5
III.	FREE ELECTRON LASER THEORY	7
A.	LORENTZ FORCE EQUATION	7
B.	ENERGY EQUATION.....	7
C.	ELECTROMAGNETIC FIELDS IN THE UNDULATOR	8
D.	UNDULATOR PARAMETER	8
E.	ELECTRON PHASE.....	9
F.	RESONANCE CONDITION	9
G.	PENDULUM EQUATION.....	10
H.	PHASE SPACE	12
I.	WEAK OPTICAL FIELDS	14
J.	STRONG OPTICAL FIELDS	15
K.	HIGH CURRENT DENSITY	16
L.	THE FEL WAVE EQUATION	18
IV.	ATMOSPHERIC PROPAGATION THEORY	21
A.	THE MASTER EQUATION	21
B.	ATMOSPHERIC EXTINCTION.....	21
C.	MOLECULAR ABSORPTION.....	22
D.	MIE SCATTERING THEORY	23
E.	BEAM DIFFRACTION	23
F.	ATMOSPHERIC TURBULENCE.....	24
G.	PLATFORM JITTER	25
H.	THERMAL BLOOMING	25
V.	FREE ELECTRON LASER AND ATMOSPHERIC PROPAGATION MODELLING	27
A.	DESCRIPTION OF FEL 4-D MODEL	27
B.	GRAPHICAL OUTPUT OF FEL 4-D MODEL.....	29
C.	DESCRIPTION OF ANCHOR	30

VI.	DESIGN OF MEGAWATT CLASS FREE ELECTRON LASERS	33
A.	DETERMINING TRANSMISSION WINDOWS	33
B.	FEL AMPLIFIER AND OSCILLATOR DESIGN	35
1.	FEL Designs for $1.0 \mu\text{m} \rightarrow 1.1 \mu\text{m}$ Transmission Window.....	36
a.	<i>FEL Amplifier Design</i>	37
b.	<i>FEL Oscillator Design</i>	40
2.	FEL Design for $1.6 \mu\text{m} \rightarrow 1.7 \mu\text{m}$ Transmission Window	42
a.	<i>FEL Amplifier Design</i>	43
b.	<i>FEL Oscillator Design</i>	44
C.	FEL AMPLIFIER AND OSCILLATOR MODELING RESULTS	45
1.	FEL Amplifier for $1.0\mu\text{m} \rightarrow 1.1\mu\text{m}$ Transmission Window	45
2.	FEL Oscillator for $1.0 \mu\text{m} \rightarrow 1.1 \mu\text{m}$ Transmission Window	48
3.	FEL Amplifier for $1.6 \mu\text{m} \rightarrow 1.7 \mu\text{m}$ Transmission Window	50
4.	FEL Oscillator for $1.6 \mu\text{m} \rightarrow 1.7 \mu\text{m}$ Transmission Window	51
VII.	PROPAGATION ANALYSIS OF MEGAWATT CLASS FREE ELECTRON LASERS.....	55
A.	PERFORMANCE METRICS	56
B.	PROPAGATION MODELING RESULTS.....	56
1.	Wavelength Sensitivity Analysis.....	56
2.	Beam Quality Sensitivity Analysis.....	61
3.	Beam Power Sensitivity Analysis.....	65
VIII.	CONCLUSION	71
LIST OF REFERENCES		73
INITIAL DISTRIBUTION LIST		75

LIST OF FIGURES

Figure 1.	Schematic diagram of superconducting Energy Recovery Linear Accelerator FEL with both amplifier and oscillator configurations.....	3
Figure 2.	Phase space plot for $0 < \tau < 1$ where initial electron phase velocity $v_0 = 0$ (i.e., at resonance).....	13
Figure 3.	Phase space plot for $0 < \tau < 1$ where initial electron phase velocity $v_0 = 2.6$ (i.e., at off-resonance).....	14
Figure 4.	Gain and phase spectrum plot in the weak optical field regime when $ a_0 = 1$	15
Figure 5.	Phase space plot in the strong optical field regime when $ a_0 = 20$	16
Figure 6.	Phase space plot at high current density when $j = 200$ and $\nu = 0$ (i.e., at resonance)	17
Figure 7.	Gain and phase spectrum plot at high current density when $j = 200$ and $\nu = 0$ (i.e., at resonance)	17
Figure 8.	Absorption spectrum in infrared region for H_2O and CO_2 ; total absorption spectrum in a tropical atmosphere.	22
Figure 9.	Plot of the $w(z)$ values as a function of z for an ideal Gaussian beam.....	24
Figure 10.	Beam profile showing thermal blooming.	26
Figure 11.	FEL 4-D model simulating an FEL oscillator configuration.....	27
Figure 12.	FEL 4-D graphical output for single pass model	29
Figure 13.	Total extinction coefficients for tropical maritime environment at altitude of 10 m above sea level.....	35
Figure 14.	Power and gain evolution for amplifier without tapering	40
Figure 15.	NPS 4-D single pass simulation results for amplifier in the $1.0 \mu\text{m} \rightarrow 1.1 \mu\text{m}$ transmission window	46
Figure 16.	NPS 4-D long pulse multi-pass simulation results for oscillator in the $1.0 \mu\text{m} \rightarrow 1.1 \mu\text{m}$ transmission window.....	48
Figure 17.	NPS 4-D single pass simulation results for amplifier in the $1.6 \mu\text{m} \rightarrow 1.7 \mu\text{m}$ transmission window	50

Figure 18.	NPS 4-D long pulse multi-pass simulation results for oscillator in the $1.6 \mu\text{m} \rightarrow 1.7 \mu\text{m}$ transmission window.....	52
Figure 19.	Peak irradiance I_p achieved on target vs. target range and altitude across lasing wavelengths $\lambda = 1064 \text{ nm}, 1073 \text{ nm}, 1550 \text{ nm}$ and 1672 nm	57
Figure 20.	Required dwell times to melt the target τ_D vs. target range and altitude across lasing wavelengths $\lambda = 1064 \text{ nm}, 1073 \text{ nm}, 1550 \text{ nm}$, and 1672 nm	59
Figure 21.	Peak irradiance I_p achieved on target vs. target range and altitude for M^2 values of 1, 3, 5, and 7.....	61
Figure 22.	Required dwell times τ_D to melt the target vs. target range and altitude for M^2 values of 1, 3, 5, and 7.....	63
Figure 23.	Peak irradiance I_p achieved on target vs. target range and altitude for beam power P of 1 MW, 800 kW, 600 kW, and 400 kW.....	66
Figure 24.	Required dwell times τ_D to melt the target vs. target range and altitude for beam power P of 1 MW, 800 kW, 600 kW, and 400 kW.....	68

LIST OF TABLES

Table 1.	Input parameters to MODTRAN for a tropical maritime environment.....	34
Table 2.	Electron beam characteristics for $1.0 \mu\text{m} \rightarrow 1.1 \mu\text{m}$ transmission window.....	37
Table 3.	Seed laser characteristics for $1.0 \mu\text{m} \rightarrow 1.1 \mu\text{m}$ transmission window.....	38
Table 4.	Amplifier undulator characteristics for $1.0 \mu\text{m} \rightarrow 1.1 \mu\text{m}$ transmission window	39
Table 5.	Oscillator undulator characteristics for $1.0 \mu\text{m} \rightarrow 1.1 \mu\text{m}$ transmission window	41
Table 6.	Optical cavity characteristics for $1.0 \mu\text{m} \rightarrow 1.1 \mu\text{m}$ transmission window.....	41
Table 7.	Electron beam characteristics for $1.6 \mu\text{m} \rightarrow 1.7 \mu\text{m}$ transmission window.....	42
Table 8.	Seed laser characteristics for $1.6 \mu\text{m} \rightarrow 1.7 \mu\text{m}$ transmission window....	43
Table 9.	Amplifier undulator characteristics for $1.6 \mu\text{m} \rightarrow 1.7 \mu\text{m}$ transmission window	44
Table 10.	Oscillator undulator characteristics for $1.6 \mu\text{m} \rightarrow 1.7 \mu\text{m}$ transmission window	44
Table 11.	Optical cavity characteristics for $1.6 \mu\text{m} \rightarrow 1.7 \mu\text{m}$ transmission window.....	45
Table 12.	Amplifier characteristics for $1.0 \mu\text{m} \rightarrow 1.1 \mu\text{m}$ transmission window	47
Table 13.	Oscillator characteristics for $1.0 \mu\text{m} \rightarrow 1.1 \mu\text{m}$ transmission window	49
Table 14.	Amplifier characteristics for $1.6 \mu\text{m} \rightarrow 1.7 \mu\text{m}$ transmission window	51
Table 15.	Oscillator characteristics for $1.6 \mu\text{m} \rightarrow 1.7 \mu\text{m}$ transmission window	53
Table 16.	ANCHOR parameters for propagation analysis	55

THIS PAGE INTENTIONALLY LEFT BLANK

LIST OF ACRONYMS AND ABBREVIATIONS

AFIT	Air Force Institute of Technology
ANCHOR	Atmospheric NPS Code for High Energy Laser Optical Propagation
DC	Direct Current
DE	Directed Energy
DOD	Department of Defense
ERL	Energy Recovery Linear Accelerator
FEL	Free Electron Laser
FWHM	Full Width Half Maximum
HEL	High Energy Laser
LEEDR	Laser Environmental Effects Definition and Reference
MIRACL	Mid-Infrared Advanced Chemical Laser
MODTRAN	Moderate Resolution Atmospheric Transmission
NPS	Naval Postgraduate School
RF	Radio Frequency
RMS	Root Mean Squared
SSL	Solid State Laser

THIS PAGE INTENTIONALLY LEFT BLANK

ACKNOWLEDGMENTS

I would like to sincerely thank Professors Joseph Blau and Keith Cohn for all of their invaluable advice, patience in instruction, and continual encouragement. You both have been key in keeping my thesis going up until completion. My heartfelt thanks goes to you both.

I would like to thank Conor Pogue for his help in getting ANCHOR working for me. You were of great help, Conor. Thank you.

I would like to thank my loving and supportive wife, Christina, for always being by my side throughout this process. I cherish you, my dear, for your timeless encouragement.

Last but not least, I would like to thank God for all of His provisions in the writing and completion of this thesis. Indeed, He has provided much and He has been good.

THIS PAGE INTENTIONALLY LEFT BLANK

I. INTRODUCTION

The development of high energy lasers (HELs) for defense against a spectrum of threats has been pursued by the U.S. Department of Defense (DOD) for decades [1]. Initial progress in megawatt class chemical lasers in the 1970s gave way to a push toward all-electric HELs using high power Free Electron Lasers (FELs). Curtailment of the Strategic Defense Initiative (SDI) in the 1990s led to a refocusing of FEL research on ship defense, cumulating in the construction of a 14 kW FEL at the Jefferson Lab in Virginia. This project was funded by the Office of Naval Research. The U.S. Navy's recent focus in the fielding of near term HEL technologies has led to the diversion of available funding to solid-state laser (SSL) programs. While SSL technology could potentially provide beam power of hundreds of kilowatts, SSLs are generally regarded as incapable of scaling up to the megawatt level.

FELs are seen as the key technology to enable scaling of HELs up to the megawatt level. Megawatt class HELs have been pursued by the DOD for their effectiveness against hardened and time-critical threats. These include sub-sonic and supersonic anti-ship cruise missiles and ballistic missiles. In the 1980s, field tests of megawatt class chemical based HELs (such as the Mid Infra-red Advanced Chemical Laser [MIRACL]¹) against cruise missiles were met with much success. Preference for an all-electric weapon led to FELs being identified as the key enabler for such megawatt HEL systems.

Our approach in this thesis is to use physics-based modeling tools to design FELs, simulate their performance, and analyze their effectiveness in a given deployment environment. In Chapter II, we begin first with an overview of the components within an FEL. In Chapter III, we move on to describe the theory behind FELs. In Chapter IV, we explain the effects of atmospheric attenuation on a propagating laser beam. In Chapter V, we give an overview of the various modeling tools used. In Chapter VI, we design and

¹ The MIRACL was a deuterium fluoride-based chemical laser developed by the U.S. Navy in the 1980s.

analyze four FEL configurations. In Chapter VII, we ascertain the effectiveness of our FEL designs. And finally in Chapter VIII, we form our conclusions.

II. OVERVIEW OF FREE ELECTRON LASERS

A schematic diagram of a high power Free Electron Laser (FEL) is seen in Figure 1. In addition, Figure 1 shows both the amplifier and oscillator FEL configurations, of which only one would be adopted in the final FEL design.

A vacuum pipe surrounds the electron path, which is shown in red. The electrons are constrained to follow this path by the use of bending magnets. At the start of the path, the cathode within the electron gun is excited to emit free electrons, which are passed into a booster. The electron gun and the booster together comprise the injector. The electrons exit the injector with energy E_i and are merged into the main beamline before they enter the linear electron accelerator (linac). Electrons exiting the linac are directed into one of the undulators and emerge from the undulator with energy $E - \Delta E$ before re-entering the linac a second time to be decelerated. The electrons are finally terminated at the beam dump. A small amount of energy ΔE is converted into laser light in the undulator.

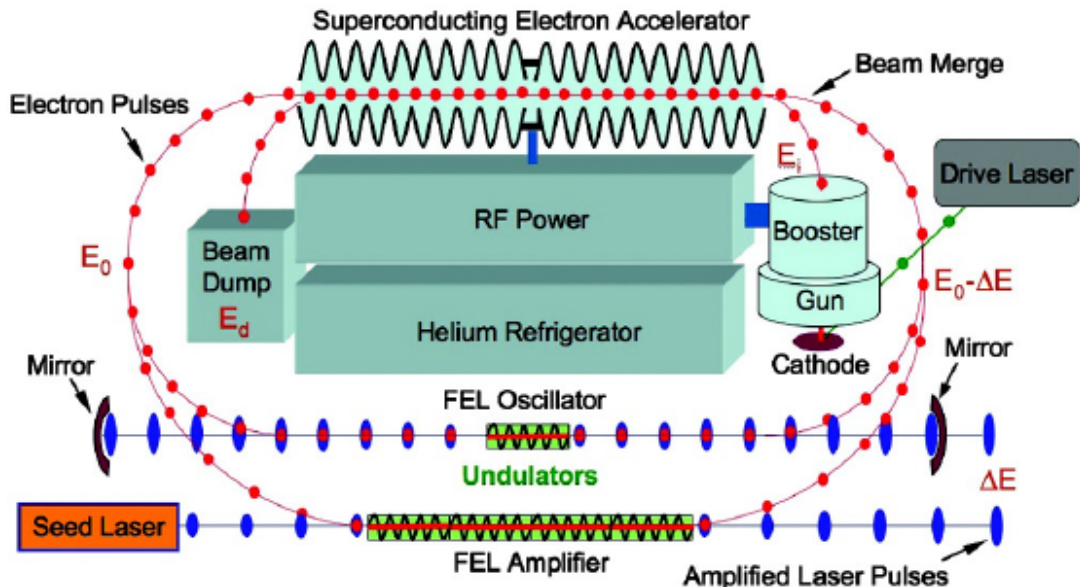


Figure 1. Schematic diagram of superconducting Energy Recovery Linear Accelerator FEL with both amplifier and oscillator configurations.
Source [2]: J. Blau et al., "High average power free-electron lasers," *Optical Eng.*, vol. 52, no. 2, pp. 021013-1 – 021013-8, Feb. 2013.

A. CATHODE

Free electrons are produced in the cathode in a continuous stream of micro-pulses. There are two technologically mature methods to produce free electrons, either by thermionic or by photoelectric means. For thermionic cathodes, heat is supplied to provide sufficient escape energy for the electrons. An alloy of tungsten and barium is often used to reduce the work function of the cathode, thus allowing more current to be produced at lower temperatures. These cathodes can last longer and have high average currents. For photocathodes, light (typically ultraviolet) from a conventional laser supplies the escape energy for the electrons. Photocathodes are characterized by their quantum efficiency (QE), which is the number of electrons emitted per incident photon. With a higher QE, photocathodes with a lower drive laser power are able to produce the same current. A trade-off is involved when selecting the QE of the photocathode. Those with a higher QE (> 0.01) usually have shorter life spans (measured in hours), while those with a lower QE ($\sim 1 \times 10^{-4}$) have longer life spans (measured in years). Photocathodes provide better control over the electron pulse profile, allowing for shorter electron bunch lengths at more precise timing and repetition rates than thermionic cathodes.

B. INJECTOR

The free electrons released from the cathode are rapidly accelerated to energies of around 5 MeV in the injector so as to prevent spreading out of the electron pulses due to Coulomb repulsion. Three possible technologies could be used for the injector. Direct current high-voltage (DCHV) injectors are not well suited for high power FELs due to their lower accelerating gradients. Normal conducting radio frequency (NCRF) injectors exhibit large ohmic losses due to cavity wall heating. Superconducting radio frequency (SRF) injectors have good vacuum and high accelerating gradients. While SRF injectors have yet to be tested at higher currents (above $\sim 1\text{mA}$ average current), they are anticipated to be the most promising technology for high average current injectors [2].

C. LINEAR ACCELERATOR

The linear accelerator further accelerates electron pulses that are in phase with the radio frequency (RF) fields to energies of around 100 MeV. Like injectors, linear accelerators come in three varieties: direct current (DC), normal conducting radio frequency (NCRF), and superconducting radio frequency (SRF) accelerators. Most experts agree that a high average power FEL would require a SRF linear accelerator to minimize resistance losses along the walls of the accelerating structure. The SRF linear accelerator stores RF fields within its niobium cavities. Superconductors require less average RF power than normal conducting accelerators. SRF linear accelerators operating in continuous wave mode produce a string of picoseconds long micro-pulses nanoseconds apart. By contrast, normal conducting linear accelerators can only operate with microseconds-long macro-pulses separated by milliseconds due to higher heat loads. This enables the SRF linear accelerator to achieve higher average power. However, there is a trade-off—a liquid helium refrigerator is needed to cool the superconductor for the SRF linear accelerator. A current outstanding research topic is the RF frequency to use for the SRF linear accelerator. Higher frequencies would reduce the size of the accelerator cavities, while frequencies below \sim 500 MHz would allow for a smaller cryo-plant. A smaller cryo-plant would reduce the system footprint and could potentially improve power efficiency.

An SRF linear accelerator that recirculates the electron beam after ΔE is extracted at the undulator is called an energy recovery linear accelerator (ERL). The recirculation recovers energy from the electron beam before it is diverted to and terminated in the beam dump. This configuration is shown in Figure 1. An ERL improves the power efficiency of the FEL by reducing the RF power. Additionally, it reduces the radiation shielding needed at the beam dump.

D. UNDULATOR AND OPTICS

Different undulators are required for the FEL oscillator and amplifier configurations. In both cases, the magnetic fields within the undulator cause the electron pulses to wiggle back and forth, resulting in the emission of laser light. In an FEL

oscillator, optical pulses are reflected back and forth between the optical cavity mirrors, resulting in a build-up of the optical field over multiple passes. Therefore, only a short undulator (~ 1 m) is needed. Care must be taken in the oscillator configuration to ensure that the electron pulses produced by the cathode are synchronized with the RF cycles in the SRF linear accelerator and the optical pulses in the cavity as the electron beam enters the undulator. In the FEL amplifier, the optical cavity is absent. Therefore, a longer undulator (~ 10 m for high power FEL) is needed since only a single pass occurs. Here, a seed laser produces optical pulses in phase with the electron pulses as they enter the undulator.

The FEL oscillator and amplifier configurations both have their merits and shortcomings. For FEL oscillators, one of the challenges faced is the possible need for active cooling of the cavity mirrors since up to ~ 100 MW of power could be directed on these mirrors. To reduce the optical power at the mirrors, another option is to design short Rayleigh length FELs where the optical beam expands more within a shorter distance, therefore allowing the beam energy to be dispersed over a larger mirror area [3]. One advantage of FEL oscillators is its greater tolerance to poor electron beam quality and misalignments due to a shorter undulator (~ 1 m).

For FEL amplifiers, a longer undulator (~ 10 m) poses a greater challenge for beam quality and alignment. In addition, unlike the FEL oscillator, a seed laser is required here, and an amplifier requires a higher quality electron beam that is more difficult to achieve. The lack of an optical cavity and its associated challenges is an advantage for the FEL amplifier.

III. FREE ELECTRON LASER THEORY

Now that we have described the key components of a Free Electron Laser (FEL), we proceed to explain how the interactions between the optical field and electron beam within the undulator generate laser light.

A. LORENTZ FORCE EQUATION

A relativistic beam of electrons of dimensionless velocity $\vec{\beta} = \frac{\vec{v}}{c}$ and Lorentz factor $\gamma = \frac{1}{\sqrt{1 - |\vec{\beta}|^2}}$ is injected into an undulator with magnetic field \vec{B} and optical field \vec{E} . The force experienced by the electrons is given by the Lorentz force equation:²

$$\frac{d(\gamma\vec{\beta})}{dt} = \frac{e}{m} \left(\frac{\vec{E}}{c} + \vec{\beta} \times \vec{B} \right), \quad (1)$$

where e and m are the charge and mass of an electron, respectively, and c is the speed of light.

B. ENERGY EQUATION

The work done on the electron $W = e \int \vec{E} \cdot \vec{v} dt$ results in a change in kinetic energy of the electron given by:

$$\Delta K = \int \frac{d}{dt} [(\gamma - 1)mc^2] dt = mc^2 \int \dot{\gamma} dt. \quad (2)$$

Equating W and ΔK , we arrive at the energy equation given by:

$$\dot{\gamma} = \frac{e}{mc} \vec{\beta} \cdot \vec{E} \quad (3)$$

² All equations are provided in S.I. units.

C. ELECTROMAGNETIC FIELDS IN THE UNDULATOR

For simplicity of calculation, we consider a helical undulator magnetic field given by $\vec{B} = B_0 [\cos(k_0 z) \hat{x} + \sin(k_0 z) \hat{y}]$ and a circularly polarized optical electric field given by $\vec{E} = E [\cos(\psi) \hat{x} - \sin(\psi) \hat{y}]$. Here, $k_0 = \frac{2\pi}{\lambda_0}$, with λ_0 being the undulator period and $\psi = kz - \omega t + \phi$, where $k = \frac{2\pi}{\lambda}$ and ϕ are the optical field wave-number and phase, respectively. The angular frequency is defined as $\omega = k c$.

Since the magnitude of the optical magnetic field is much smaller than the undulator magnetic field, it is ignored in our calculations. Starting with the Lorentz force in equation (1) and substituting the expressions \vec{B} for the helical undulator and \vec{E} for the circularly polarized optical field, we arrive at the following expressions for the change in transverse and longitudinal dimensionless velocity $\vec{\beta}$:

$$\frac{d(\gamma \vec{\beta}_\perp)}{dt} = \frac{-e}{m} [-\beta_z B_0 \sin(k_0 z) \hat{x} + \beta_z B_0 \cos(k_0 z) \hat{y}], \quad (4)$$

$$\frac{d(\gamma \beta_z)}{dt} = \frac{-e}{m} \left\{ \beta_x \left[B_0 \sin(k_0 z) + \frac{E}{c} \cos(\phi) \right] - \beta_y \left[B_0 \cos(k_0 z) + \frac{E}{c} \sin(\phi) \right] \right\}. \quad (5)$$

Here we make the assumption that the electron beam is highly relativistic and travelling primarily in the z direction (i.e., $\beta_z \approx 1$).

D. UNDULATOR PARAMETER

Assuming $\dot{\gamma} \approx 0$ and $z = ct$, we integrate equation (4) to obtain:

$$\vec{\beta}_\perp = \frac{-K}{\gamma} [\cos(k_0 z) \hat{x} + \sin(k_0 z) \hat{y}], \quad (6)$$

where K is the dimensionless undulator parameter given by:

$$K = \frac{e B_0 \lambda_0}{2\pi m c}. \quad (7)$$

Typically, $K \approx 1$.

E. ELECTRON PHASE

Starting with the energy equation (3) and substituting in the expression \vec{E} for the circularly polarized optical field and $\vec{\beta}_\perp$ given in equation (6), we arrive at the expression given by:

$$\dot{\gamma} = \frac{eKE}{\gamma mc} \cos(\zeta + \phi), \quad (8)$$

where ζ is the ‘electron phase’ and is given by:

$$\zeta = (k_0 + k)z - \omega t. \quad (9)$$

It can be seen in equation (12) that for a relativistic beam of electrons, γ is large, and hence, $\lambda \ll \lambda_0$ where λ_0 and λ are the undulator period and optical wavelength, respectively. This implies that $k_0 = \frac{2\pi}{\lambda_0} \ll k = \frac{2\pi}{\lambda}$. Using this relation, the electron phase approximates to $\zeta \approx \frac{2\pi}{\lambda}z - \omega t$, and we can see that ζ describes the position of the electron on the scale of an optical wavelength.

F. RESONANCE CONDITION

At constant electron phase, $\dot{\zeta} \approx 0$. Taking $z = \beta_z ct$ and approximating $\dot{\beta}_z \approx 0$, we differentiate equation (9) to obtain:

$$\lambda = \frac{\lambda_0(1-\beta_z)}{\beta_z} \approx \lambda_0(1-\beta_z). \quad (10)$$

The above approximation can be made since we assume a highly relativistic beam of electrons (i.e. $\beta_z \approx 1$). Next, we recall that the Lorentz factor $\gamma^{-2} = 1 - |\vec{\beta}|^2$, where $|\vec{\beta}|^2 = \beta_x^2 + \beta_y^2 + \beta_z^2$. Defining $|\vec{\beta}_\perp|^2 = \beta_x^2 + \beta_y^2$, we substitute equation (6) into the

expression $\gamma^{-2} = 1 - |\vec{\beta}|^2$ to obtain $\gamma^{-2} = 1 - \frac{K^2}{\gamma^2} - \beta_z^2$. Expressing this equation in terms of β_z , we get:

$$\beta_z = \sqrt{1 - \frac{(1+K^2)}{\gamma^2}} \approx 1 - \frac{(1+K^2)}{2\gamma^2}. \quad (11)$$

We are able to ignore the higher order terms due to $\frac{1+K^2}{\gamma^2} \ll 1$. Substituting equation (11) into equation (10), we now obtain the resonance condition given by:

$$\lambda = \frac{\lambda_0(1+K^2)}{2\gamma^2}. \quad (12)$$

The resonance condition tells us the approximate optical wavelength λ emitted for a given electron energy γmc^2 , undulator period λ_0 , and undulator parameter K when operating at resonance.

G. PENDULUM EQUATION

We define a dimensionless time $\tau = \frac{ct}{L}$ for an undulator of length L . Here, when $0 < t < \frac{L}{c}$, $0 < \tau < 1$, thus $\tau = 0$ occurs at the start of the undulator, and $\tau = 1$ occurs at the end of the undulator. The dimensionless time derivative is expressed as $\dot{\square} \equiv \frac{d}{d\tau} \square = \frac{L}{c} \frac{d}{dt} \square$. The phase velocity, v , is defined as $v = \frac{d\zeta}{d\tau}$. Differentiating equation (9) with respect to τ and setting $z = \beta_z ct$, we arrive at the following expression:

$$v = L[(k_0 + k)\beta_z - k]. \quad (13)$$

A phase velocity of zero (i.e. $v = 0$) corresponds to resonance. To find \dot{v} , we differentiate equation (13) with respect to τ and, assuming $k \ll k_0$, we obtain:

$$\overset{\circ}{\nu} = \frac{L^2}{c} k \dot{\beta}_z. \quad (14)$$

Differentiating equation (11) to obtain $\dot{\beta}_z = (1+K^2) \frac{\dot{\gamma}}{\gamma^3}$ and rearranging equation (12) to obtain $k = 2\pi \left[\frac{2\gamma^2}{\lambda_0(1+K^2)} \right]$, we substitute $\dot{\beta}_z$ and k into equation (14) to obtain:

$$\overset{\circ}{\nu} = \frac{L}{c} 4\pi N \frac{\dot{\gamma}}{\gamma}. \quad (15)$$

Here, N is the number of undulator periods, and it is given by $N = \frac{L}{\lambda_0}$. From equation (15) we can also derive the following expression:

$$\Delta\nu = 4\pi N \frac{\Delta\gamma}{\gamma}. \quad (16)$$

Since the kinetic energy of an electron is given by $(\gamma - 1)mc^2$, $\Delta\gamma$ relates directly to a change in the electron kinetic energy. In order for the optical field to grow, the electrons need to lose energy. Therefore, $\Delta\gamma$ should be negative, and thus, $\Delta\nu$ should also be negative. More specifically, the average change in ν over an electron bunch $\langle \Delta\nu \rangle$ has to be negative for an FEL to work. Here, $\langle \rangle$ corresponds to the averaging function.

In addition, if we differentiate equation (13) with respect to λ and substitute $\lambda = \lambda_0(1 - \beta_z)$ into the expression, we get:

$$\Delta\nu = 2\pi N \frac{\Delta\lambda}{\lambda}. \quad (17)$$

This tells us that a change in electron phase velocity would also result in a change in the emitted optical wavelength.

Finally, we substitute the expression for $\dot{\gamma}$ in equation (8) into equation (15) to obtain the pendulum equation given by:

$$\ddot{\zeta} = \overset{\circ}{\nu} = |a| \cos(\zeta + \phi). \quad (18)$$

Here, $|a|$ is the amplitude of the dimensionless optical field given by:

$$|a| = \frac{4\pi NeKL|E|}{\gamma^2 mc^2} . \quad (19)$$

H. PHASE SPACE

The trajectories of the electrons can be better understood by plotting them in phase space, (ζ, v) . The electrons orbit the phase space diagram as prescribed by the pendulum equation in (18). The separatrix in the phase space diagram separates the electrons that undergo closed orbits from those that have open orbits. Electrons inside the separatrix undergo closed orbits, while electrons outside it undergo open orbits. The equation for the separatrix is given by:

$$v^2 = 2|a|[1 + \sin(\zeta + \phi)] \quad (20)$$

It can be seen that the separatrix is dependent on the optical field amplitude $|a|$ and the optical phase ϕ , both of which will evolve as the electrons traverse through the undulator.

Figure 2 shows the phase space plot of the electrons injected into the undulator with $v = 0$ (i.e., at resonance). It can be seen that at $\tau = 1$, electron bunching occurs at $\zeta = \pi/2$. Half of the electrons gain energy (i.e., $\Delta v > 0$), while half of the electrons lose energy (i.e., $\Delta v < 0$). Hence, $\langle \Delta v \rangle \approx 0$ and no net energy is transferred to the optical field. In this case, the FEL would not work. In Figure 2, the electrons transition from the color yellow at $\tau = 0$ to red at $\tau = 1$.

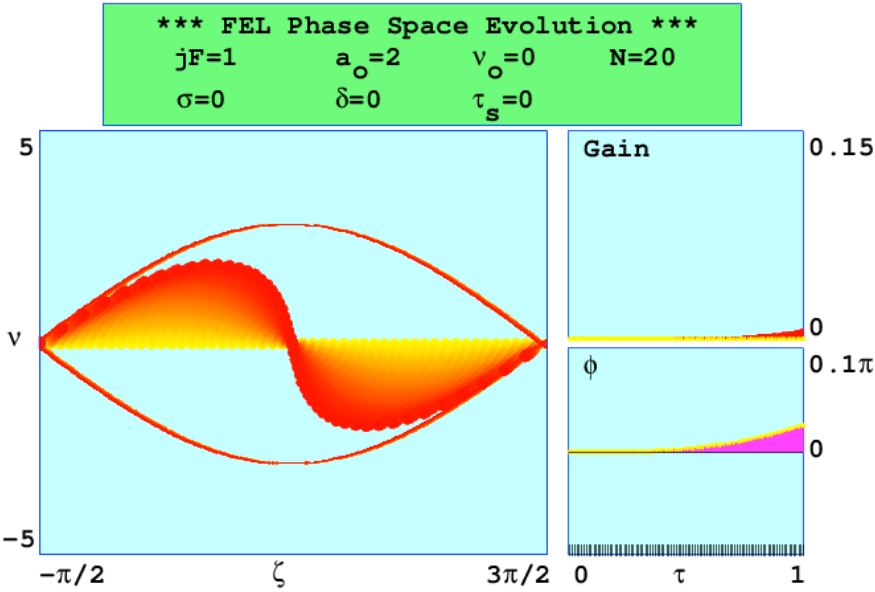


Figure 2. Phase space plot for $0 < \tau < 1$ where initial electron phase velocity $v_0 = 0$ (i.e., at resonance)

In the next example, we inject electrons into the undulator with $v > 0$ (i.e., slightly off resonance). We can see from Figure 3 that now there are more electrons that lose energy than those that gain energy. Therefore, $\langle \Delta v \rangle < 0$ and there is net energy transferred to the optical field. In addition, bunching of electrons occurs at $\zeta = \pi$, promoting the emission of coherent light.

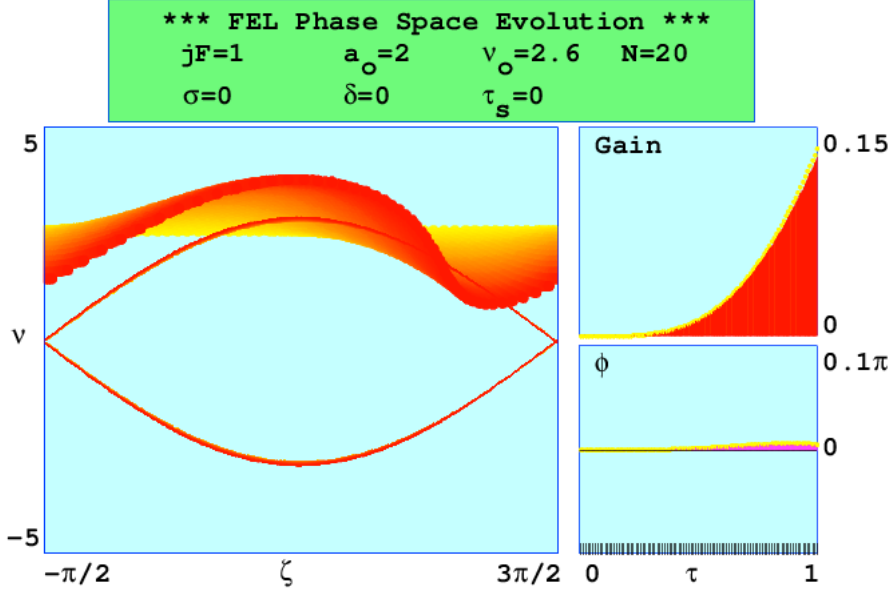


Figure 3. Phase space plot for $0 < \tau < 1$ where initial electron phase velocity $v_0 = 2.6$ (i.e., at off-resonance)

I. WEAK OPTICAL FIELDS

As mentioned in equation (19), the dimensionless optical field amplitude is given by $|a|$. Under weak optical field conditions in the undulator, $|a| \ll \pi$. We can see from the pendulum equation in (18) that this leads to a small change in the electron's phase velocity. The gain experienced by the optical field when $|a| \ll \pi$ is given by:

$$G = \frac{j}{v_0^3} [2 - 2 \cos(v_0\tau) - v_0\tau \sin(v_0\tau)] . \quad (21)$$

This is called the weak field gain formula and corresponds to the yellow line in the “Gain” plot in Figure 3. Here, v_0 is the average initial phase velocity of the electrons. The parameter j is the dimensionless current density given by:

$$j = \frac{2\pi Ne^2 K^2 L^2 \rho}{\gamma^3 mc^2 \epsilon_0} . \quad (22)$$

The electron density is expressed as ρ , and the permittivity of free-space is given by ϵ_0 . The weak field gain formula in equation (21) is only valid for $j < \pi$. A plot of the weak field gain formula in equation (21) against v_0 as seen in Figure 4 tells us that no gain occurs when $v_0 = 0$ (i.e., at resonance). This is consistent with our previous conclusion that when $v_0 = 0$, phase space plots show that $\langle \Delta v \rangle = 0$ and no net energy is transferred to the optical field. Additionally, we see from Figure 4 that maximum weak field gain occurs when $v_0 \approx 2.6$.

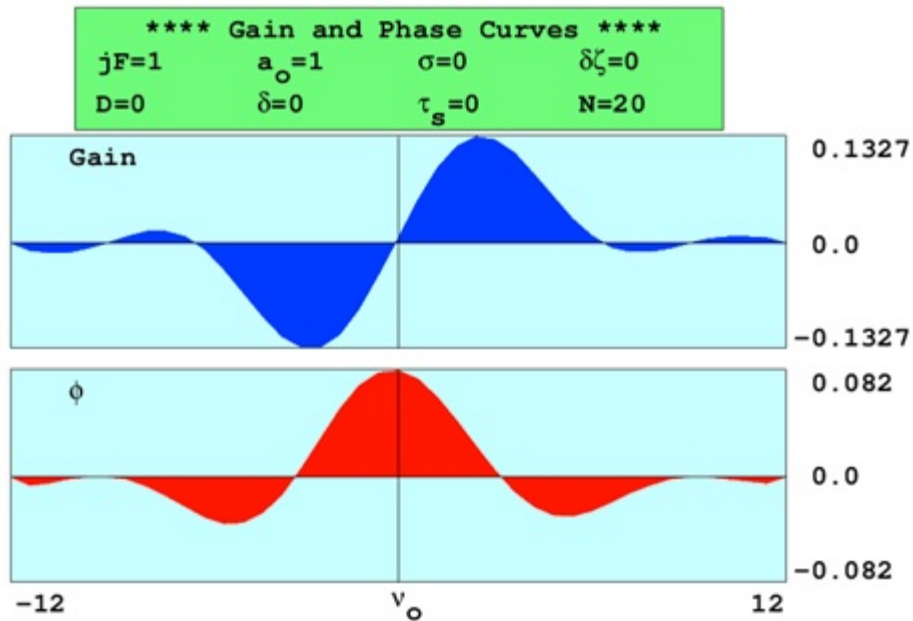


Figure 4. Gain and phase spectrum plot in the weak optical field regime when $|a_0|=1$

J. STRONG OPTICAL FIELDS

When $|a| \geq \pi$, the FEL enters the strong optical field regime. We can see from Figure 5 that a strong optical field can result in ‘over-bunching’ of electrons in phase space. The over-bunched electrons start to move upwards in phase space (i.e., their average v increases), and they gain energy at the expense of the optical field, thereby leading to saturation in the gain. This can be seen in Figure 5, where the simulated gain

(as seen in red in the ‘Gain’ plot) plateaus off and deviates from the theoretical weak field gain formula curve, as seen in the yellow line.

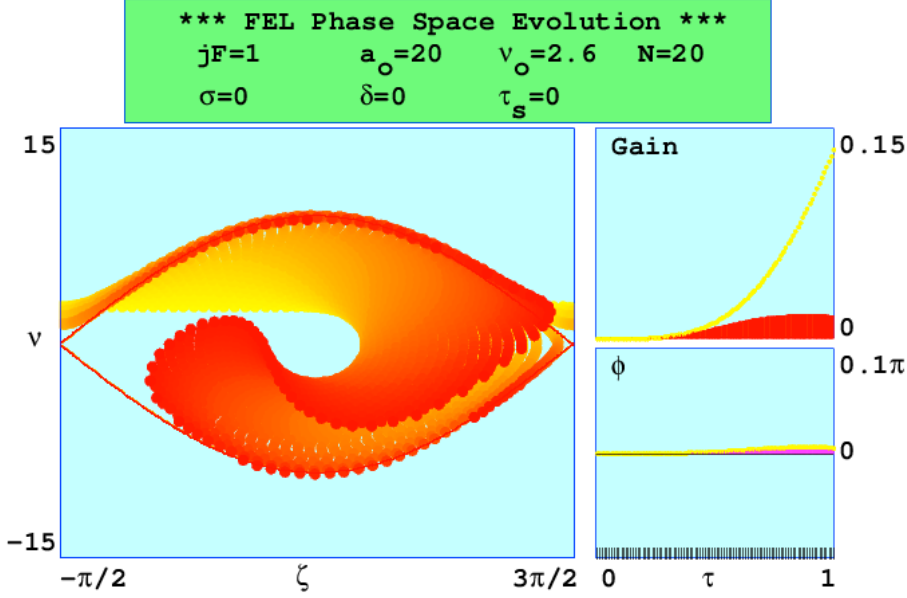


Figure 5. Phase space plot in the strong optical field regime when $|a_0| = 20$

K. HIGH CURRENT DENSITY

At high current densities, the dimensionless current density is increased such that $j \gg \pi$. This results in a significant increase in the optical field amplitude $|a|$ and shift in optical phase ϕ as seen in Figure 6. We remember from equation (20) that the peak-to-peak height of the separatrix is given by $4|a|$. Hence an increase in the peak to peak separatrix height corresponds to an increase in $|a|$. Additionally, we observe from Figure 7 that significant gain now occurs even when $v = 0$ (i.e., at resonance). A shift in the separatrix occurs due to the optical phase shift, and the electrons are now bunched at the ‘optimum’ phase relative to the separatrix.

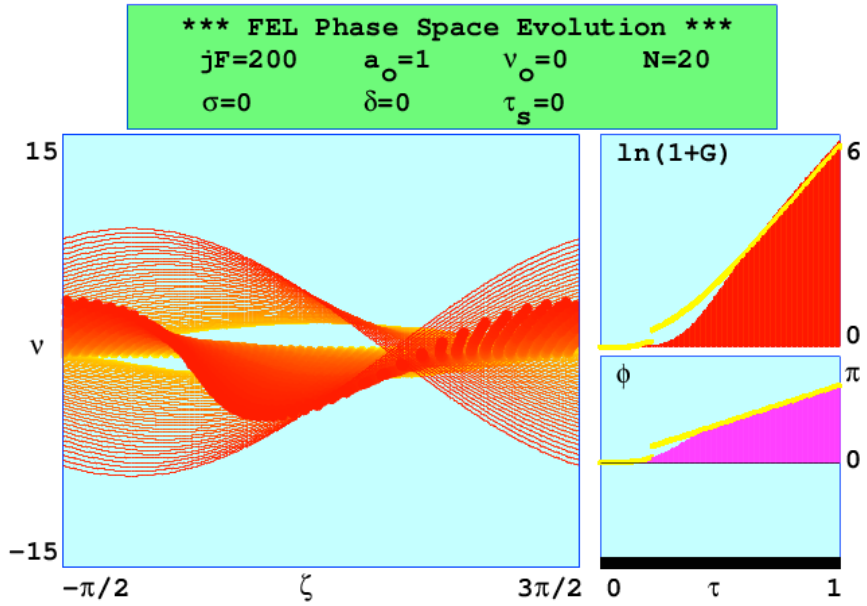


Figure 6. Phase space plot at high current density when $j = 200$ and $v = 0$ (i.e., at resonance)

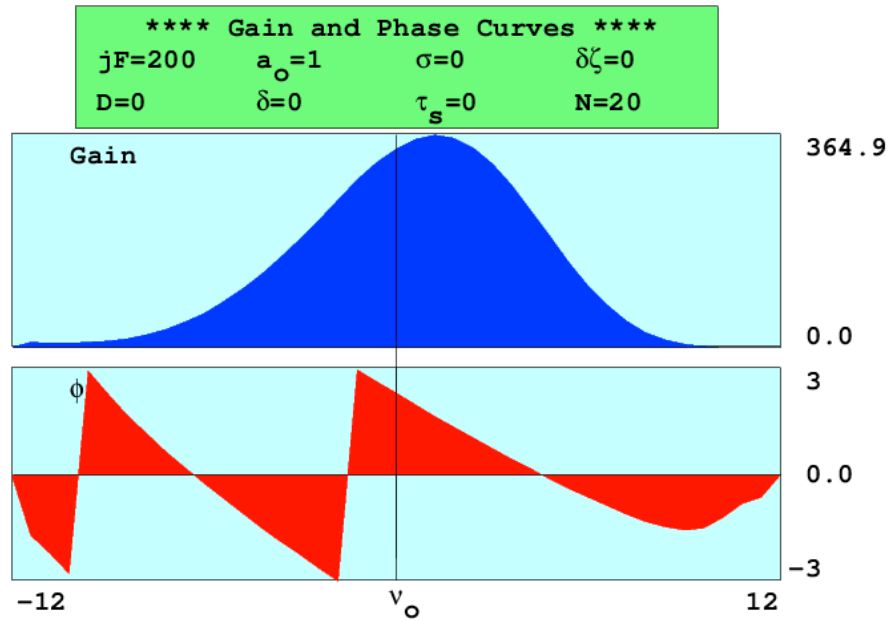


Figure 7. Gain and phase spectrum plot at high current density when $j = 200$ and $v = 0$ (i.e., at resonance)

L. THE FEL WAVE EQUATION

Now that we have described electron motion in the undulator, we turn our attention to how the optical field evolves in the undulator. We start with a general three-dimensional wave equation given by:

$$\left(\nabla^2 - \frac{1}{c^2} \frac{\partial^2}{\partial t^2} \right) \vec{A}(\vec{r}, t) = -\mu_0 \vec{J}_\perp(\vec{r}, t). \quad (23)$$

Here, $\vec{A}(\vec{r}, t)$ refers to the wave vector potential and $\vec{J}_\perp(\vec{r}, t)$ refers to the current density in the transverse direction given by:

$$\vec{J}_\perp = -e c \sum_i \vec{\beta}_\perp \delta(\vec{r} - \vec{r}_i). \quad (24)$$

We assume the following solution for equation (23):

$$\vec{A}(\vec{r}, t) \approx \vec{A}(z, t) = \frac{E(z, t)}{\omega} e^{i(kz - \omega t)} (-i \hat{x} + \hat{y}). \quad (25)$$

Thus, we assume that the optical field experiences no transverse dependence and the resultant optical field is circularly polarized.

Performing partial differentiation on $\vec{A}(z, t)$ with respect to the spatial and temporal dimensions yields equations (26) and (27), respectively:

$$\frac{\partial^2 \vec{A}}{\partial z^2} = \left(2ik \frac{\partial E}{\partial z} - k^2 E + \frac{\partial^2 E}{\partial z^2} \right) \frac{e^{i(kz - \omega t)}}{\omega} (-i \hat{x} + \hat{y}), \quad (26)$$

$$\frac{\partial^2 \vec{A}}{\partial t^2} = \left(-2i\omega \frac{\partial E}{\partial t} - \omega^2 E + \frac{\partial^2 E}{\partial t^2} \right) \frac{e^{i(kz - \omega t)}}{\omega} (-i \hat{x} + \hat{y}). \quad (27)$$

We now invoke the slowly-varying envelope approximation, which assumes that there is no significant change in $|a|$ and ϕ over an optical wavelength. In addition, we see that k and ω in equations (26) and (27), respectively, are large numbers. Hence, we

can set $\frac{\partial^2 E}{\partial z^2} \approx \frac{\partial^2 E}{\partial t^2} \approx 0$. Combining equations (26) and (27) with equation (23), we arrive at the following expression:

$$2ik\left(\frac{\partial}{\partial z} + \frac{1}{c}\frac{\partial}{\partial t}\right)E = -\mu_0 [\vec{J}_\perp \cdot (i\hat{x} + \hat{y})] \omega e^{-i(kz - \omega t)}. \quad (28)$$

Now, we choose to follow a single slice of the optical field as it traverses the undulator, and we are able to remove the $\frac{\partial}{\partial z}$ dependence in equation (28).

Starting with equation (6) for $\vec{\beta}_\perp$, we arrive at the following equation:

$$\vec{\beta}_\perp = \text{Re} \left[\frac{-K}{\gamma} ie^{-ik_0 z} (-i\hat{i} + \hat{j}) \right]. \quad (29)$$

Substituting equation (29) into equation (24) and then into equation (28), we arrive at the following expression:

$$\frac{\partial E}{\partial t} = -\frac{1}{2} \mu_0 (ec^3 K \rho) \left\langle \frac{e^{-i[(k+k_0)z - \omega t]}}{\gamma} \right\rangle. \quad (30)$$

Note that we have replaced the sum of individual electron charge and positions in equation (24) with their average over all electrons multiplied by the electron density ρ . We recall that the electron phase is $\zeta = (k+k_0)z - \omega t$. Converting to dimensionless units and simplifying, we finally arrive at the FEL wave equation:

$$\overset{\circ}{a} = -j \left\langle e^{-i\zeta} \right\rangle \quad (31)$$

Here, a is the dimensionless optical field we have already defined in equation (19) and j is the dimensionless current density as defined in equation (22). Using the FEL wave equation in equation (31), we find the amplitude of the optical field evolves as:

$$\left| \overset{\circ}{a} \right| = -j \left\langle \cos(\zeta + \phi) \right\rangle. \quad (32)$$

Assuming $\phi = 0$, when the electrons first arrive at the undulator, they are spread uniformly over ζ space, hence $\langle \cos(\zeta) \rangle = 0$ and there is no change in the optical field amplitude. We can see that maximum increase in the optical field amplitude occurs when $\zeta = \pi$ and $\left| \overset{\circ}{a} \right| = -j \langle \cos(\pi) \rangle = j$. This is consistent with what we observed in Figure 3, whereby electron bunching at $\zeta = \pi$ leads to a significant gain in the optical field.

The evolution of the optical field phase $\overset{\circ}{\phi}$ is given by:

$$\overset{\circ}{\phi} = \frac{j \langle \sin(\zeta + \phi) \rangle}{|a|}. \quad (33)$$

It can be seen that a significant shift in the optical phase would occur at high current densities when $j \gg \pi$. This is illustrated in Figure 6 where the separatrix shifts towards the left when the current density $j = 200$.

IV. ATMOSPHERIC PROPAGATION THEORY

As the laser light propagates through the atmosphere, attenuation occurs. We briefly cover the key phenomenon that together determine the final power delivered to the target.

A. THE MASTER EQUATION

The time-averaged irradiance $\langle I \rangle$ delivered to the target is estimated by the following master equation:

$$\langle I \rangle \approx \frac{P_0}{\pi \langle w_{total} \rangle^2} e^{-\varepsilon z} S_{TB}. \quad (34)$$

Here, P_0 is the output power at the beam director, z is the distance to target, ε is the total extinction coefficient due to atmospheric absorption and scattering, and $\langle w_{total} \rangle$ is the time-averaged laser spot radius on the target. This spot radius combines the effects of beam diffraction, atmospheric turbulence, and platform jitter and is given by

$$\langle w_{total} \rangle^2 = w_d^2 + w_t^2 + w_j^2, \quad (35)$$

where w_d , w_t , and w_j are the contributions from diffraction, turbulence, and jitter, respectively. Finally, S_{TB} is the thermal blooming Strehl ratio.

B. ATMOSPHERIC EXTINCTION

Atmospheric molecules and aerosols scatter and/or absorb light. This phenomenon is known as atmospheric attenuation and is described by Beer's law,

$$P(z) = P_0 e^{-\varepsilon z} \quad (36)$$

where P_0 and ε are as previously described, P is the power delivered to the target plane, and z is the distance the beam travels. The extinction coefficient ε is made up of four components:

$$\varepsilon = \alpha_m + \alpha_a + \beta_m + \beta_a. \quad (37)$$

Here, α and β refer to the absorption and scattering coefficients, respectively, and the subscripts m and a refer to molecular and aerosol³ contributions, respectively.

C. MOLECULAR ABSORPTION

Molecular absorption is accounted for by the coefficient α_m . Although the atmosphere is comprised primarily of nitrogen (N_2 ; 78%) and oxygen (O_2 ; 21%), carbon dioxide (CO_2 ; 0.04%) and water vapor (H_2O ~1%) dominate the molecular absorption spectrum in the infrared region, as seen in Figure 8. These results are measured experimentally and can also be derived through quantum theory, which we do not cover here.

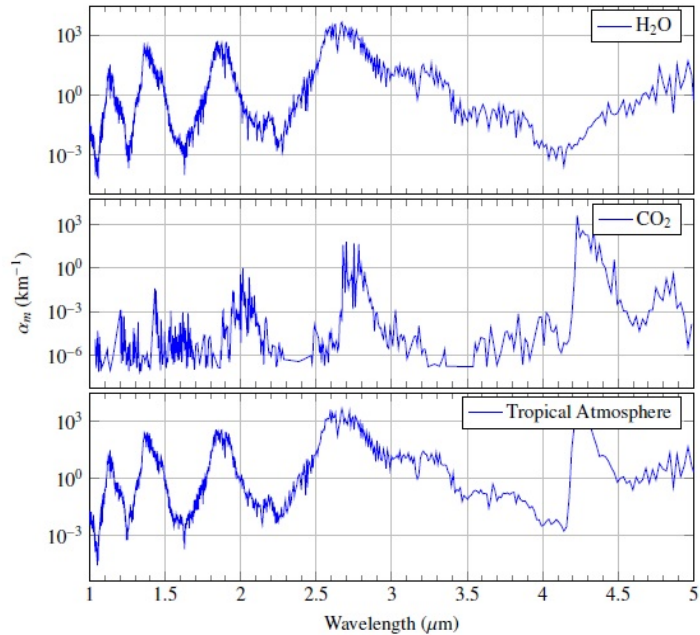


Figure 8. Absorption spectrum in infrared region for H_2O and CO_2 ; total absorption spectrum in a tropical atmosphere. The top and middle insets show the α_m values for H_2O and CO_2 molecules, respectively. Their dominance of the total absorption spectrum in a tropical atmosphere is seen in the bottom inset. Data is obtained from HITRAN database.

³ Aerosols comprise mixtures of solid particles and/or liquid droplets suspended in the atmosphere. Examples of natural aerosols are fog, haze, and dust.

D. MIE SCATTERING THEORY

The Mie scattering theory is used to estimate the extinction coefficients α_a , β_m , and β_a . Assuming that the incident optical field is a plane wave and the molecules/aerosols are spherical with a constant index of refraction, we are able to calculate the far-field effects of the scattered light and arrive at the scattering σ_s and absorption σ_a cross sections unique to each molecule/aerosol type. Multiplying σ_s or σ_a with the number density of particles in the atmosphere N gives us their associated extinction coefficients $\alpha = N\sigma$. When the light wavelength λ is much larger than the particle size, we find that shorter wavelengths undergo scattering much more readily. This phenomenon is known as Rayleigh scattering.

The atmospheric extinction coefficients α_m , β_m , α_a , and β_a for a specific geographic location at a specified time and altitude are usually extracted from atmospheric modeling software. Examples of such software are the Laser Environmental Effects Definition and Reference (LEEDR) software developed by the Center of Directed Energy (CDE) at the Air Force Institute of Technology (AFIT) and Moderate Resolution Atmospheric Transmission (MODTRAN) developed by Spectral Sciences Inc. and the Air Force Research Laboratory.

E. BEAM DIFFRACTION

The irradiance of an ideal Gaussian beam is given by:

$$I(r, z) = I_0 \left[\frac{w_0}{w(z)} \right]^2 e^{-2 \frac{r^2}{w^2(z)}}. \quad (38)$$

Here, I_0 is the irradiance at the center of the beam waist ($z = 0$), r is the radial distance from the optical axis, z is the distance along the optical axis, and $w(z)$ is the radial distance from the optical axis where the irradiance drops by a factor of $1/e^2$ measured as a function of z , given by the following equation [4]:

$$w(z) = w_0 \sqrt{1 + \left(\frac{z}{z_R}\right)^2}. \quad (39)$$

The beam waist w_0 occurs at the origin of the z axis. The Rayleigh range is given by

$z_R = \frac{\pi w_0^2}{\lambda}$, where λ is the optical wavelength. As illustrated in Figure 9, z_R is the distance from the beam waist where the beam radius expands by a factor of $\sqrt{2}$.

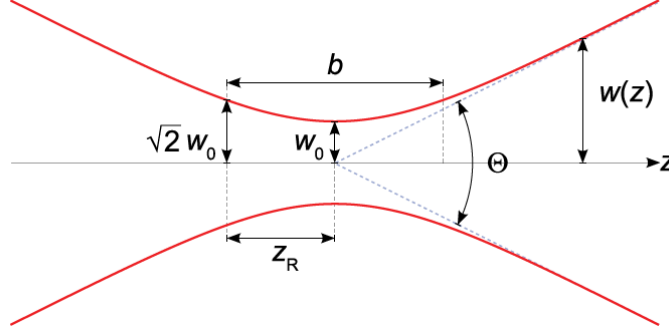


Figure 9. Plot of the $w(z)$ values as a function of z for an ideal Gaussian beam

From equation (39), we are able to estimate the spot radius due to diffraction given by:

$$w_d = M^2 \frac{2\lambda z}{\pi D}. \quad (40)$$

Here, z is the distance to target, D is the diameter of the beam director, and M^2 is the beam quality factor. For an ideal Gaussian beam, $M^2 = 1$. For non-ideal beams, $M^2 > 1$.

F. ATMOSPHERIC TURBULENCE

Atmospheric turbulence arises from random temperature variations in the atmosphere. This leads to variations in density and, hence, localized changes in the refractive index, ultimately resulting in wavefront distortion and ‘speckling.’ Turbulence is quantified by the refractive structure constant C_n^2 with units $[\text{length}]^{-2/3}$; this is usually measured experimentally or characterized using atmospheric modeling software

like LEEDR. The refractive structure constant tends to vary significantly with altitude — it usually decreases with increasing altitude. The values of C_n^2 typically range from $10^{-17}[\text{length}]^{-2/3}$ for weak turbulence to $10^{-13}[\text{length}]^{-2/3}$ for strong turbulence.

With C_n^2 , we can now calculate the value of the Fried parameter r_0 . This is the diameter over which the beam maintains transverse coherence throughout its propagation length. For constant C_n^2 , it is given by:

$$r_0 = 0.33 \frac{\lambda^{6/5}}{l^{3/5} (C_n^2)^{3/5}}. \quad (41)$$

If r_0 is larger than D , the beam maintains coherence over its entire diameter. However, if r_0 is smaller than D , the beam breaks up into beamlets over its propagation length. In this case, the spot radius due to turbulence would be given by:

$$w_t = \frac{2\lambda l}{\pi r_0}. \quad (42)$$

G. PLATFORM JITTER

Platform motion, vibration and tracking errors introduce jitter to the laser spot's position. The time averaged-radius of the spot due to jitter is given by:

$$w_j \approx \theta_{rms} l \quad (43)$$

Here, θ_{rms} is the angular variance due to jitter. A value of θ_{rms} for a typical system would be of the order of a few μrad .

H. THERMAL BLOOMING

Thermal blooming effects are taken into account by the thermal blooming Strehl's ratio S_{TB} , which is the fractional degradation of irradiance due to thermal blooming. Thermal blooming occurs due to heating of air along the beam propagation path. Heating results from absorption of light by atmospheric particles and is directly related to α_m and

α_a . Air density of the warming air drops, and thus, the refractive index is modified across the beam, resulting in the creation of a ‘de-focusing lens.’ The formation of this ‘lens’ results in a drop in beam irradiance near the center of the optical beam axis, thereby significantly reducing the optical power delivered to the target. This effect is illustrated in Figure 10 where the left inset shows the longitudinal profile of the optical beam irradiance throughout its propagation path and the right insert shows the transverse profile of the optical beam irradiance at the target. Thermal blooming results in the creation of a ‘donut’ shaped transverse irradiance profile as seen in the right insert. The effects of thermal blooming are quantified by calculating the steady-state phase shift of the optical beam due to isobaric heating effects. These isobaric heating effects take into account laser heating and heat removal due to convection (i.e., wind) and conduction. Wind plays a significant role here. A cross wind would bring in cooler air, resulting in a reduction of the thermal blooming effects.

The thermal blooming Strehl’s ratio S_{TB} can be estimated empirically or using modeling tools.

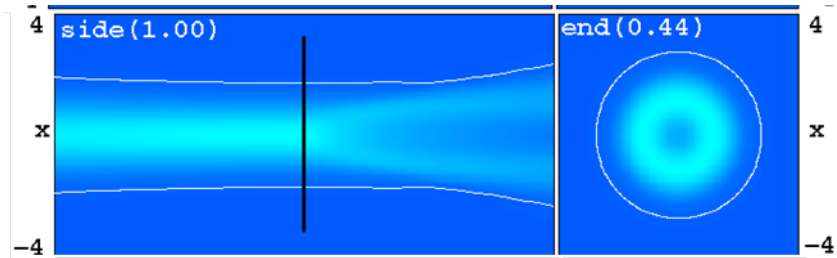


Figure 10. Beam profile showing thermal blooming

V. FREE ELECTRON LASER AND ATMOSPHERIC PROPAGATION MODELLING

In order to better understand the evolution of the electron and optical pulses in the undulator, the Naval Postgraduate School (NPS) has developed several computer programs that model FEL behavior. Of interest here is the NPS 4-dimensional (4-D) FEL model that simulates both FEL oscillators and amplifiers.

In addition, in order to account for the atmospheric losses in a propagating optical beam and calculate the irradiance on target, NPS developed ANCHOR, which stands for Atmospheric NPS Code for High Energy Laser Optical Propagation. ANCHOR can be used for all types of high energy lasers (HEL) and is not limited to FELs.

A. DESCRIPTION OF FEL 4-D MODEL

The 4-D model is a high-fidelity simulation that describes the evolution of the electron and optical pulses in (x, y, z, t) space. A 3-D grid consisting of typically 300 by 300 points in the transverse (x and y) directions and typically 100 points in the longitudinal (z) direction follows the electron and optical pulses as they traverse the undulator. The evolution of these pulses is shown in Figure 11.

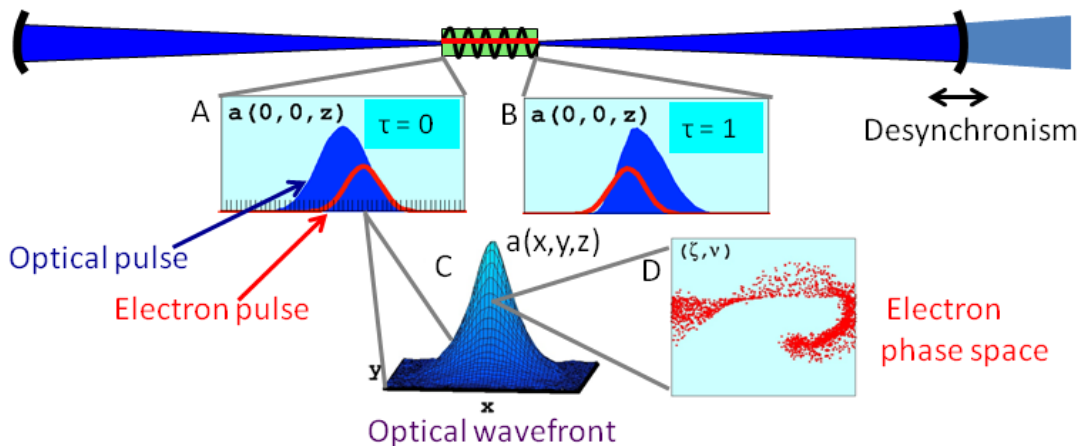


Figure 11. FEL 4-D model simulating an FEL oscillator configuration

Here, the distributions of the optical field amplitude (in blue) and electron density (in red) along a longitudinal slice of the 3-D grid is seen at the beginning of the undulator, $\tau = 0$ (as pictured in inset A), and at the end of the undulator, $\tau = 1$ (as pictured in inset B). The electron pulse moves towards the rear of the optical pulse since the electrons travel slower than the speed of light. This pulse slippage produces a distorted resultant optical field. The ability to account for such short pulse effects is one key advantage of the 4-D model.

A transverse slice of the 3-D grid is pictured in inset C, showing the optical amplitude as a function of (x, y) . This model allows asymmetrical and multi-mode optical profiles to be simulated. Each grid point is populated with sample electrons in phase space (as seen in inset D), where the electron phase space coordinates and optical field amplitude evolve according to the pendulum equation in (18) and the FEL wave equation in (31), respectively.

The 4-D model consists of several versions—a single pass model, a long pulse multi-pass model, and a short pulse multi-pass model. The single pass model is used for FEL amplifiers to simulate the electron and optical pulse evolving through a single pass of the undulator.

The long pulse multi-pass model assumes periodic boundary conditions along the z axis (i.e., uniform electron density and initial optical field amplitude). This is used for FEL oscillators where the pulse length is much greater than the pulse slippage distance. An expanding coordinate grid outside the undulator accounts for optical diffraction. A transformation matrix is used to represent the cavity mirrors. The self-contained optics allows the long pulse multi-pass simulation model to run efficiently.

The short pulse multi-pass model does away with the periodic boundary conditions and models the full profile of the electron density and optical amplitude profile within the longitudinal window. The short pulse model takes into account pulse slippage effects. The out-coupling mirror of the optical cavity can be shifted inwards to account for pulse lethargy. This mirror shift is known as desynchronization and is shown in Figure 11.

B. GRAPHICAL OUTPUT OF FEL 4-D MODEL

The graphical output generated from the single pass model is shown in Figure 12. The graphical output for the other two models are nearly identical to the single pass model, except the evolution is shown over many passes instead of a single pass.

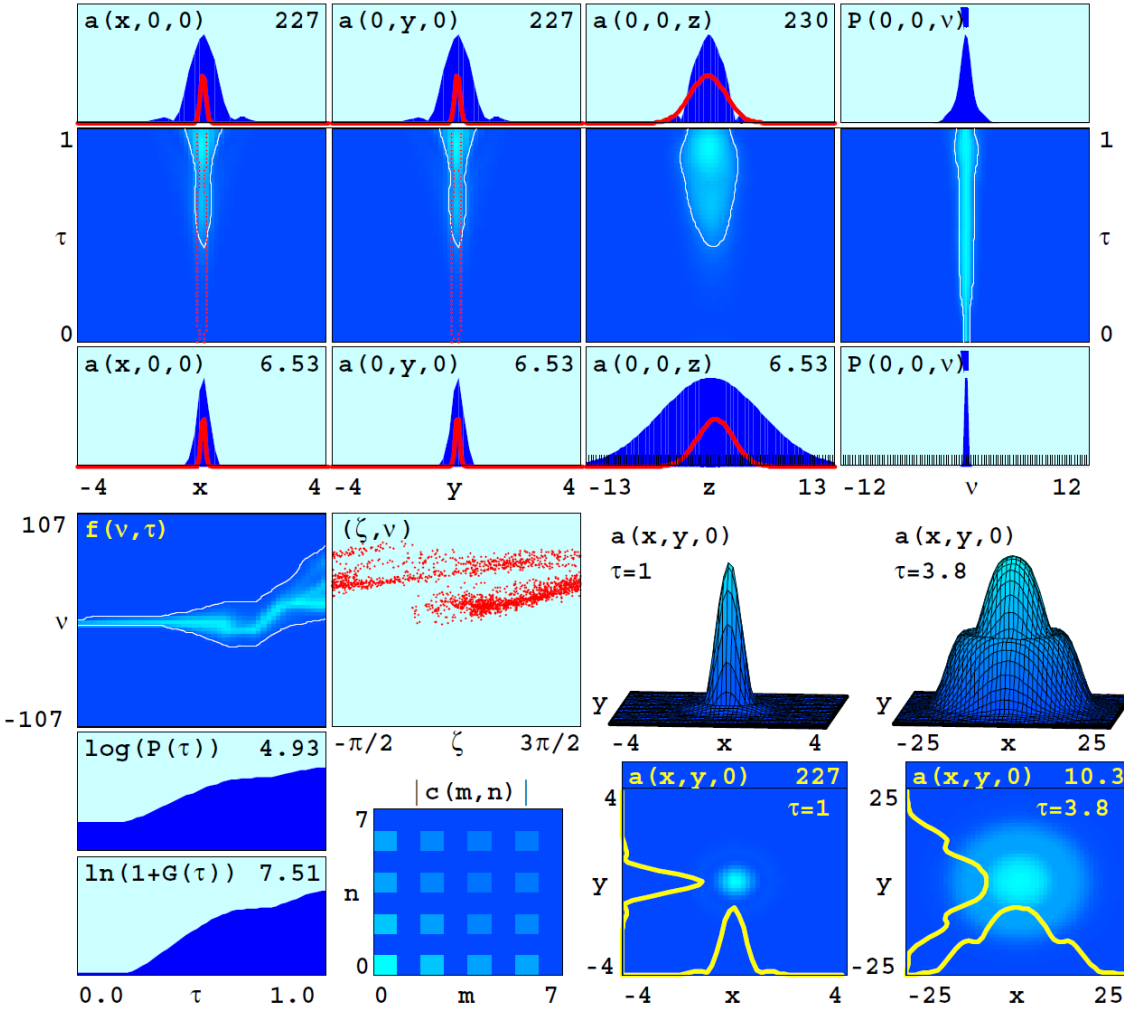


Figure 12. FEL 4-D graphical output for single pass model

The top half of the graphical output contains four columns with three rows, where the first three columns from the left show the x , y , and z cross-sections of the optical and electron pulses in blue and red, respectively. The bottom row shows the cross-sections at the beginning of the undulator ($\tau = 0$), and the top row shows them at the end

of the undulator ($\tau = 1$). In between the x , y , and z cross-sections is the evolution of the optical pulse along the x , y , and z directions as it traverses the undulator from $\tau = 0$ to $\tau = 1$. Here, a light blue color represents a larger optical field amplitude $|a|$. Notice that the dimensionless optical field amplitude $|a|$ grows from 6 when $\tau = 0$ to over 200 when $\tau = 1$ in the x , y , and z directions. The rightmost column shows the evolution of the optical power as a function of the electron phase velocity v . Since a change in v would result in a change in the emitted optical wavelength (see equation (17)), this insert shows the power spectrum of the emitted optical wavelength.

For the bottom half of the graphical output, we proceed to explain the insets by going in a clockwise manner starting with the top left inset. This inset shows the evolution of the phase velocity distribution $f(v, \tau)$, where a high electron density is indicated in light blue. The next inset shows the phase space plot of the electrons at $\tau = 1$. The next four plots show the optical field magnitude $|a|$ at $\tau = 1$ and at an arbitrary point of interest outside of the undulator. The next inset shows the Hermite-Gaussian modes of the optical beam at $\tau = 1$. The final insets in the lower left show the evolution of power and gain achieved by the system.

C. DESCRIPTION OF ANCHOR

The HEL propagation model, ANCHOR, is able to model HEL propagation under a variety of atmospheric conditions. It takes into consideration all of the associated attenuation phenomenon as described in Section IV. This propagation model is written as a Matlab script and uses atmospheric extinction coefficients extracted from atmospheric characterization software such as LEEDR and MODTRAN. This propagation model consists of three versions. The first is a simplified version called ANCHORS, which calculates the average irradiance on target at a given range. This simplified model assumes constant atmospheric extinction coefficients, turbulence, and wind along the given path and is useful for horizontal engagements. The other two versions, ANCHORL and ANCHORP, do not assume constant atmospheric conditions. ANCHORL generates a

vertical slice through a given engagement volume showing how the average irradiance on target varies with altitude. ANCHORP generates a horizontal slice through a given engagement volume showing how the average irradiance on target varies with azimuth.

Power-in-the-bucket is defined as the total power that falls on a target within a circular area of radius r_b . This is found by integrating the irradiance of the beam over the circular area of radius r_b . Dwell time is the time taken for the laser spot to melt a given cylindrical volume of target material as defined by the radius r_b and thickness t . Dwell time takes into consideration power input as calculated by power-in-the-bucket, power loss due to conduction and radiation mechanisms, and energy required to melt the given target material. Both power-in-the-bucket and dwell time are outputs from all three versions of the propagation model. Together, the average irradiance on target, power-in-the-bucket, and dwell time provide us with the necessary metrics to determine laser beam lethality for a given target.

A key feature of ANCHOR is its use of scaling laws to simulate HEL propagation, thus allowing it to run much faster than industry-standard propagation codes such as WaveTrain. Beam diffraction is scaled as a function of the propagation distance. Turbulence is scaled as a function of the ratio of D/r_0 , where D is the diameter of the beam director and r_0 is the Fried parameter. Scaling of thermal blooming is done using the Strehl ratio S_{TB} . The Strehl ratio is defined as the ratio of I/I_{TB} , where I is the peak beam irradiance taking into account diffraction, turbulence, and jitter, while I_{TB} is the peak beam irradiance taking into account thermal blooming in addition to diffraction, turbulence, and jitter.

THIS PAGE INTENTIONALLY LEFT BLANK

VI. DESIGN OF MEGAWATT CLASS FREE ELECTRON LASERS

The objective of this thesis is to design and analyze the performance of high power FELs. Our goal here is to develop megawatt class FEL designs in both amplifier and oscillator configurations and analyze their effectiveness in a given deployment environment.

The design goal is achieved in two steps. First, we have to select suitable wavelengths for the FELs to lase at. This is done by determining the atmospheric transmission windows in the given deployment environment across a range of possible lasing wavelengths. Second, we then proceed to optimize the parameters of the amplifier and oscillator FELs for each suitable lasing wavelength. These tasks are accomplished using MODTRAN to ascertain the transmission windows and the NPS 4-D FEL model to simulate the outcomes of each set of design parameters.

Analysis of the FEL effectiveness is also done in two steps. First, we simulate beam propagation through a given atmosphere for the designed FELs. Second, with the beam characteristics at the target, we then calculate the various performance metrics pertaining to lethality of the FEL on a given target. Both these tasks are accomplished using ANCHOR.

This chapter covers FEL design, while the subsequent chapter covers FEL effectiveness analysis.

A. DETERMINING TRANSMISSION WINDOWS

In order to maximize FEL beam power on target, minimum atmospheric attenuation is desirable. A tropical maritime deployment environment was chosen and MODTRAN⁴ was used as our atmospheric characterization software to generate the propagation extinction coefficients. The following parameters as shown in Table 1 are representative of a tropical maritime environment and were used as input to MODTRAN.

⁴ MODTRAN is widely used and accepted in industry to generate atmospheric propagation coefficients.

Table 1. Input parameters to MODTRAN for a tropical maritime environment

Parameter	Type/Value Chosen	Comments	MODTRAN Input
Atmospheric model	Tropical Atmosphere	Valid up to 15° Latitude	MODEL = 1
Aerosol model	Maritime model	Default meteorological range set to 23km	IHAZE = 4
Rain model	No rain	Clear day	ICLD = 0
Visibility	Default	Visibility of 23km	VIS = 23
Temperature	300 K	Temperature at sea level. Varies with altitude according to atmospheric model.	MODEL = 1
Absolute Humidity	19.7 g/m ³ (80% relative humidity)	Humidity at sea level. Varies with altitude according to atmospheric model.	MODEL = 1

With this input to MODTRAN, the extinction coefficients for the wavelengths of 1 μm to 5 μm were generated. The wavelength range of 1 μm to 5 μm was selected due to the availability of suitable transmission windows within this range of wavelengths and physical limitations on the size of the FEL and the beam director. Figure 13 shows the total extinction coefficients (sum of α and β values for molecules and aerosols) over the wavelengths of 1 μm to 5 μm at an altitude of 10 m above sea level.

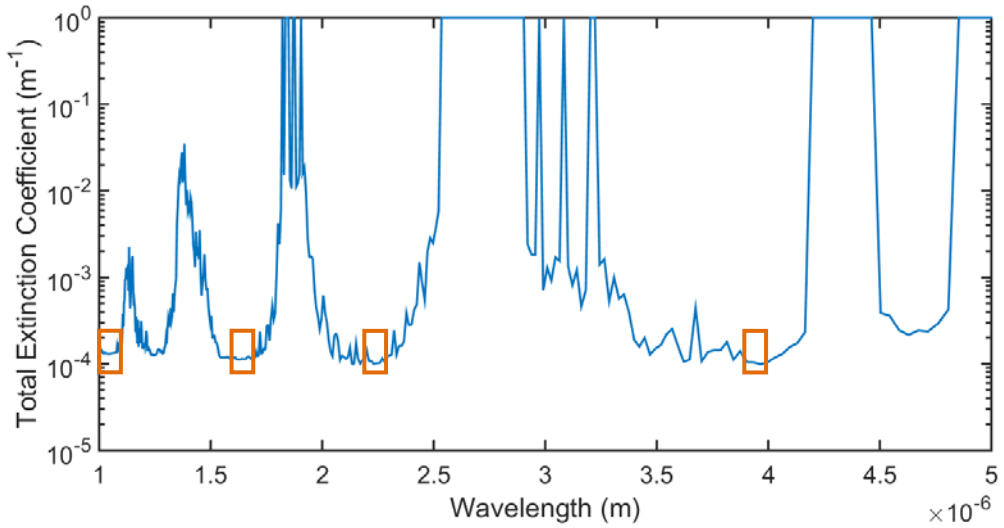


Figure 13. Total extinction coefficients for tropical maritime environment at altitude of 10 m above sea level. The four boxes drawn indicate suitable transmission windows.

Four suitable transmission windows, each with a total extinction coefficient on the order of magnitude of 10^{-4} m^{-1} , were chosen. These four transmission windows with approximate wavelengths of $1.0 \mu\text{m} \rightarrow 1.1 \mu\text{m}$, $1.6 \mu\text{m} \rightarrow 1.7 \mu\text{m}$, $2.2 \mu\text{m} \rightarrow 2.3 \mu\text{m}$, and $3.9 \mu\text{m} \rightarrow 4.0 \mu\text{m}$ are indicated in the boxes drawn in Figure 13.

While FEL oscillators can be designed to lase over a broad range of wavelengths, this is not so for FEL amplifiers. FEL amplifiers require the use of a seed laser, and this imposes limitations on the available wavelengths the FEL amplifier can lase at. Due to the unavailability of suitable seed lasers in the $2.2 \mu\text{m} \rightarrow 2.3 \mu\text{m}$ and $3.9 \mu\text{m} \rightarrow 4.0 \mu\text{m}$ wavelengths, we were unable to design FEL amplifiers to match these transmission windows. Since it is of interest to compare the effectiveness of both amplifier and oscillator designs in each transmission window, we focus only on the wavelengths $1.0 \mu\text{m} \rightarrow 1.1 \mu\text{m}$ and $1.6 \mu\text{m} \rightarrow 1.7 \mu\text{m}$, where seed lasers are available and therefore both amplifier and oscillator designs can be realized.

B. FEL AMPLIFIER AND OSCILLATOR DESIGN

In order to perform an ‘apples-to-apples’ comparison between the effectiveness of the amplifier and oscillator designs, identical injectors and linear accelerators were used

for both types of FELs for each transmission window. The undulator and optical characteristics were optimized according to the requirements for an amplifier or oscillator design. For the FEL amplifier designs, suitable seed lasers were chosen to match the given transmission windows as closely as possible. The key goal here was to achieve an FEL with an output beam power of at least 1 MW for both amplifier and oscillator designs in both transmission windows.

1. FEL Designs for $1.0 \mu\text{m} \rightarrow 1.1 \mu\text{m}$ Transmission Window

For this transmission window, we designed the injector and linear accelerator to provide us with an electron beam with the following characteristics as shown in Table 2. In order to achieve lasing in the $1.0 \mu\text{m} \rightarrow 1.1 \mu\text{m}$ window, we chose an electron beam energy of 100 MeV. A bunch charge of 1 nC and pulse repetition frequency of 500 MHz were used to scale up the average electron beam power to 50 MW. A parabolic shaped pulse with duration of 2 picoseconds was chosen. Since there are currently no linear accelerators with these parameters, the values of emittance and beam energy spread were chosen based on reasonable estimates of how such an injector and linear accelerator could perform. Additionally, we are constrained by how large the emittance and energy spread can be before the FEL performance is significantly affected. Amplifiers are especially susceptible to large beam energy spreads and emittance due to the large resulting phase velocity spread of the electrons as they pass through the amplifier undulator, which is usually one or two orders of magnitude longer than the oscillator undulator. This larger phase velocity spread would reduce the effectiveness of electron bunching, thereby lowering extraction. Hence, we chose to cap the beam energy spread at 0.1% in order to make our design goal achievable. A more conservative value of 10 mm mrad for the x and y emittance was chosen.

Table 2. Electron beam characteristics for $1.0 \mu\text{m} \rightarrow 1.1 \mu\text{m}$ transmission window

Parameter	Value
Beam Kinetic Energy	100 MeV
Bunch Charge	1 nC
Pulse Shape	Parabolic
Pulse Duration (full width half maximum)	2 ps
Pulse Repetition Frequency	500 MHz
Normalized x Emittance (rms)	10 mm mrad
Normalized y Emittance (rms)	10 mm mrad
Beam Energy Spread (rms)	0.1%
Average Beam Power	50 MW

In order to achieve our desired output optical beam power of 1 MW, an extraction efficiency η of at least 2% is needed. This means that at least 2% of the average electron beam power must be converted into optical power.

a. FEL Amplifier Design

A lasing wavelength of 1064 nm was chosen for this design due to the availability of commercial-off-the-shelf (COTS) seed lasers with the same lasing wavelength. The characteristics of the seed laser are specified in Table 3. The seed laser pulse duration was designed to be twice the length of the electron pulse duration in order to achieve an effective overlap for the interaction of the seed laser optical pulse and the electron pulse. While there exist seed lasers which lase at 1064 nm, we were unable to find a COTS product with the required pulse duration, pulse repetition frequency and peak power as given in Table 3. However, for the purposes of this thesis, we will assume that such a seed laser is available.

Table 3. Seed laser characteristics for $1.0 \mu\text{m} \rightarrow 1.1 \mu\text{m}$ transmission window

Parameter	Value
Pulse Shape	Parabolic
Pulse Duration (full width half maximum)	4 ps
Pulse Repetition Frequency	500 MHz
Peak Power	230 kW
Wavelength	1064 nm

The amplifier undulator was designed with the parameters as shown in Table 4. The physical size of the magnets used in the undulator limit how closely they can be spaced and, hence, how short each undulator period length can be. Since only a single pass occurs in an amplifier a long undulator is needed in order to increase interactions between the electron beam and the undulator magnetic field. The value of the undulator gap was varied in order to achieve a resonance wavelength that matched the seed laser wavelength.

Table 4. Amplifier undulator characteristics for $1.0 \mu\text{m} \rightarrow 1.1 \mu\text{m}$ transmission window

Parameter	Value
Undulator Period Length	3 cm
Number of Periods	200
Undulator Gap	1.162 cm
Undulator Parameter K (rms)	1.32
Taper Start Location along Undulator	270 cm
Taper Rate	-200 G/m

For an amplifier, tapering has to be performed to optimize extraction. As the electrons pass through the long amplifier undulator, overbunching causes the FEL gain to saturate. We recall that the resonance wavelength λ_R is given by the equation

$$\lambda_R = \frac{\lambda_0(1+K^2)}{2\gamma^2}.$$

Through interaction with the electromagnetic fields in the undulator,

the electrons lose energy, and their γ decreases. In order to maintain the resonance condition, we compensate by decreasing the K value accordingly. This is done by decreasing the magnetic field strength along the undulator and is referred to as tapering.

Taper optimization was performed by varying the taper start location and taper rate. The optimization process was done in the following way. First, the simulation was done using the FEL 4-D single pass model without any tapering. The power and gain evolution obtained, as shown in Figure 14, saturated at $\tau \approx 0.5$ as indicated by the red line. This was used as the initial estimate for the taper start location τ_s .

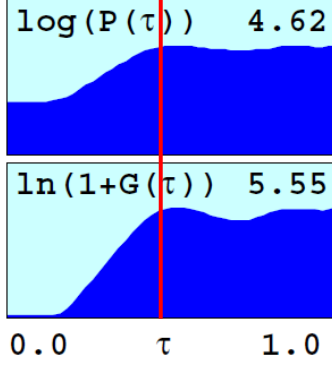


Figure 14. Power and gain evolution for amplifier without tapering

The range of desirable taper rates is given by the following formula:

$$\frac{4|a|^{\frac{1}{2}}}{1-\tau_s} \leq \delta < \frac{|a|}{1-\tau_s} \quad (44)$$

where $|a|$ is the optical field amplitude at saturation, δ is the linear taper rate, and τ_s is the taper start location. An initial estimate for the linear taper rate δ_s was taken to be

$\frac{4|a|^{\frac{1}{2}}}{1-\tau_s}$. With the initial taper start location τ_s and initial taper rate δ_s , multiple

simulations were run over a range of values for τ_s and δ_s to obtain the peak value for extraction. The taper start location and taper rate shown in Table 4 correspond to the maximum extraction observed from these runs; these correspond to the dimensionless values of $\tau_s = 0.45$ and $\delta_s = 65\pi$.

b. FEL Oscillator Design

The oscillator undulator was designed with the parameters as shown in Table 5.

Since extraction can be estimated by $\eta = \frac{1}{2N}$, where N is the number of undulator periods, we decrease N in order to increase η . However, lowering N also decreases the dimensionless current density j as shown in equation (22), which in turn reduces the system gain G as shown in equation (21). An optimal value of N was chosen based on

these considerations. The value of the undulator gap was varied in order to achieve a resonance wavelength that falls within the transmission window of $1.0 \mu\text{m} \rightarrow 1.1 \mu\text{m}$.

Table 5. Oscillator undulator characteristics for $1.0 \mu\text{m} \rightarrow 1.1 \mu\text{m}$ transmission window

Parameter	Value
Undulator Period Length	3 cm
Number of Periods	16
Undulator Gap	1.2 cm
Undulator Parameter K (rms)	1.27

The oscillator optical cavity was designed with the following parameters as shown in Table 6. A long cavity length and short Rayleigh range were chosen to keep the mirror optical intensity below 200 kW/cm^2 . The mirror quality factor Q was optimized based on the following considerations. The lower bound of Q was chosen such that the gain was greater than the losses per pass, while the upper bound of Q was chosen such that the mirror optical intensity did not exceed 200 kW/cm^2 .

Table 6. Optical cavity characteristics for $1.0 \mu\text{m} \rightarrow 1.1 \mu\text{m}$ transmission window

Parameter	Value
Cavity Length	30 m
Rayleigh Range	4.8 cm
Mirror Quality Factor	6
Optical Intensity at Mirrors	186 kW/cm^2

2. FEL Design for $1.6 \mu\text{m} \rightarrow 1.7 \mu\text{m}$ Transmission Window

For this transmission window, we designed the injector and linear accelerator to provide us with an electron beam with the following characteristics as shown in Table 7. Since lasing occurs at longer wavelengths of $1.6 \mu\text{m} \rightarrow 1.7 \mu\text{m}$, we lowered the beam energy to 80 MeV. The rest of the parameters remain identical to the injector and linear accelerator configuration for the $1.0 \mu\text{m} \rightarrow 1.1 \mu\text{m}$ window.

The average beam power now drops to 40 MW since we are lasing at a longer wavelength. Hence, in order to achieve our desired output optical beam power of 1 MW, an extraction η of at least 2.5% is desired. With this in mind, we proceeded to design the undulator and optics for the amplifier and oscillator.

Table 7. Electron beam characteristics for $1.6 \mu\text{m} \rightarrow 1.7 \mu\text{m}$ transmission window

Parameter	Value
Beam Kinetic Energy	80 MeV
Bunch Charge	1 nC
Pulse Shape	Parabolic
Pulse Duration (full width half maximum)	2 ps
Pulse Repetition Frequency	500 MHz
Normalized x Emittance (rms)	10 mm mrad
Normalized y Emittance (rms)	10 mm mrad
Beam Energy Spread (rms)	0.1%
Average Beam Power	40 MW

a. FEL Amplifier Design

A lasing wavelength of 1550 nm was chosen for this design due to the availability of COTS seed lasers with the same lasing wavelength. Although this does not fall within the $1.6 \mu\text{m} \rightarrow 1.7 \mu\text{m}$ transmission window, this lasing wavelength presents the closest match to the transmission window. The characteristics of this seed laser are specified in Table 8. The parameters are identical to the seed laser specified for the $1.0 \mu\text{m} \rightarrow 1.1 \mu\text{m}$ window except for the lasing wavelength. Similarly, here, while there exist seed lasers which lase at 1550 nm, we were unable to find a COTS product with the required pulse duration, pulse repetition frequency and peak power as given in Table 8. However, for the purposes of this thesis, we will assume that such a seed laser is available.

Table 8. Seed laser characteristics for $1.6 \mu\text{m} \rightarrow 1.7 \mu\text{m}$ transmission window

Parameter	Value
Pulse Shape	Parabolic
Pulse Duration (full width half maximum)	4 ps
Peak Power	230 kW
Wavelength	1550 nm

The amplifier undulator was designed with the parameters as shown in Table 9. Only the undulator period length and the number of periods remain identical to the amplifier for the $1.0 \mu\text{m} \rightarrow 1.1 \mu\text{m}$ window. The value of the undulator gap was varied in order to achieve a resonance wavelength that matched the seed laser wavelength. A similar process of taper optimization was done by varying the taper start location and taper rate in order to achieve maximum extraction. The taper start location and taper rate shown in Table 9 correspond to the maximum extraction observed from these runs; these correspond to the dimensionless values of $\tau_s = 0.4$ and $\delta_s = 75\pi$.

Table 9. Amplifier undulator characteristics for $1.6 \mu\text{m} \rightarrow 1.7 \mu\text{m}$ transmission window

Parameter	Value
Undulator Period Length	3 cm
Number of Periods	200
Undulator Gap	1.212 cm
Undulator Parameter K (rms)	1.25
Taper Start Location along Undulator	240 cm
Taper Rate	-162 G/m

b. FEL Oscillator Design

The oscillator undulator was designed with the parameters as shown in Table 10. The undulator period length and number of periods remain identical to the oscillator in the $1.0 \mu\text{m} \rightarrow 1.1 \mu\text{m}$ window. Similarly, the value of the undulator gap was varied in order to achieve a resonance wavelength which falls within the transmission window of $1.6 \mu\text{m} \rightarrow 1.7 \mu\text{m}$.

Table 10. Oscillator undulator characteristics for $1.6 \mu\text{m} \rightarrow 1.7 \mu\text{m}$ transmission window

Parameter	Value
Undulator Period Length	3 cm
Number of Periods	16
Undulator Gap	1.21 cm
Undulator Parameter K (rms)	1.25

The optical cavity is designed with the following parameters as shown in Table 11. The optical cavity has identical parameters to the oscillator in the $1.0\text{ }\mu\text{m} \rightarrow 1.1\text{ }\mu\text{m}$ window. The reduction in the mirror optical intensity is a result of the longer optical wavelength within the cavity that, due to diffraction, results in a larger spot on the mirrors.

Table 11. Optical cavity characteristics for $1.6\text{ }\mu\text{m} \rightarrow 1.7\text{ }\mu\text{m}$ transmission window

Parameter	Value
Cavity Length	30 m
Rayleigh Range	4.8 cm
Mirror Quality Factor	6
Optical Intensity at Mirrors	96 kW/cm ²

C. FEL AMPLIFIER AND OSCILLATOR MODELING RESULTS

The NPS 4-D single pass model and the long pulse multi-pass model were used to simulate the amplifier and oscillator designs, respectively. As the electron beam pulse length is more than 20 times the pulse slippage distance for the modeled oscillators, the long pulse multi-pass model was chosen over the short pulse multi-pass model. All four designs have an optical output power in excess of 1 MW and achieve lasing at the desired wavelengths.

1. FEL Amplifier for $1.0\mu\text{m} \rightarrow 1.1\mu\text{m}$ Transmission Window

The simulation results of the amplifier for the $1.0\mu\text{m} \rightarrow 1.1\mu\text{m}$ transmission window are shown in Figure 15.

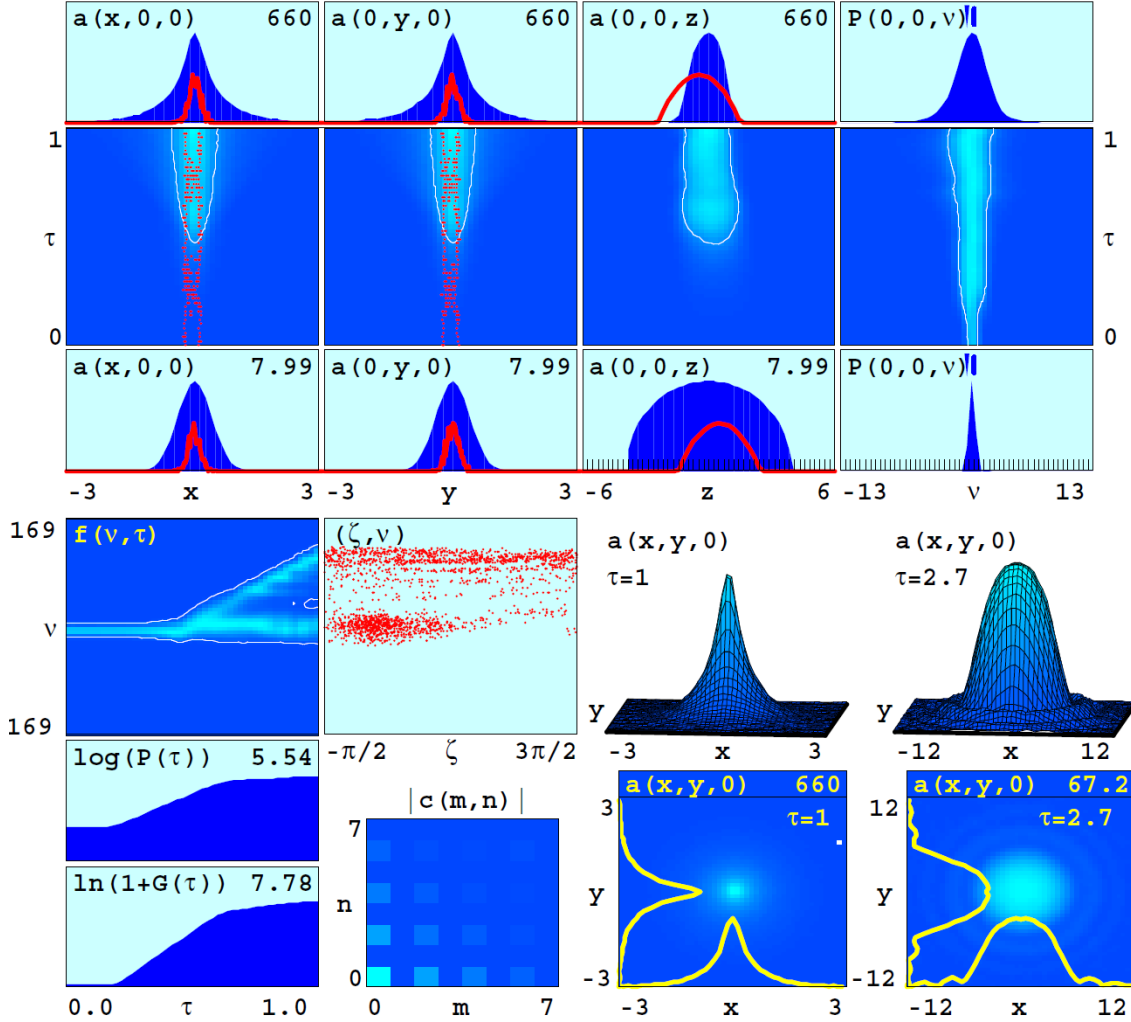


Figure 15. NPS 4-D single pass simulation results for amplifier in the $1.0 \mu\text{m} \rightarrow 1.1 \mu\text{m}$ transmission window

From the inset showing the evolution of optical power as a function of electron phase velocity $P(0,0,v)$ against τ (top right), we see that although the wavelength of the optical spectrum peak has not changed, the spectrum width has increased. This indicates that while lasing still occurs at the seed laser wavelength, the linewidth has increased. From the inset showing the evolution of phase velocity distribution $f(v,\tau)$ (middle left), we can see a distinct segregation of electrons to after the taper is applied at $\tau = 0.45$. After $\tau = 0.45$, approximately half of the electrons remain trapped inside the

separatrix near resonance at $\nu \approx 0$, while half become untrapped far off resonance at $\nu \approx 150$. In addition, from the inset showing the final phase space plot of the electrons at $\tau = 1$ (middle center), we can also see a distinct separation between electrons with a higher phase velocity and those with a lower phase velocity. Both of these indicate that tapering has been applied at the optimal location and tapering rate with approximately half the electrons losing their energy to the optical beam. From the inset showing the evolution of power and gain against τ (bottom left), we see that both power and gain continue to increase beyond $\tau = 0.45$, further indicating that optimal tapering has been applied to delay saturation. The inset showing the Hermite-Gaussian modes indicates poor beam quality with multiple non-fundamental modes present.

The characteristics of the modeled amplifier are given in Table 12. The lasing linewidth is calculated using $\Delta\nu = 2\pi N \frac{\Delta\lambda}{\lambda}$, where N is the number of undulator periods and λ is the resonant wavelength. The amplifier is able to achieve a small linewidth due to a large value of N . With this linewidth, the amplifier is still able to lase within the $1.0 \mu\text{m} \rightarrow 1.1 \mu\text{m}$ window. An extraction of 2.05% allows us to achieve an average optical beam power of 1.025 MW, which exceeds our target of 1 MW.

Table 12. Amplifier characteristics for $1.0 \mu\text{m} \rightarrow 1.1 \mu\text{m}$ transmission window

Parameter	Value
Extraction	2.05%
Lasing wavelength	$1.064 \mu\text{m}$
Lasing Linewidth (full width half maximum)	3.5 nm
Average Optical Beam Power	1.025 MW

2. FEL Oscillator for $1.0 \mu\text{m} \rightarrow 1.1 \mu\text{m}$ Transmission Window

The simulation results of the oscillator for the $1.0 \mu\text{m} \rightarrow 1.1 \mu\text{m}$ transmission window are shown in Figure 16.

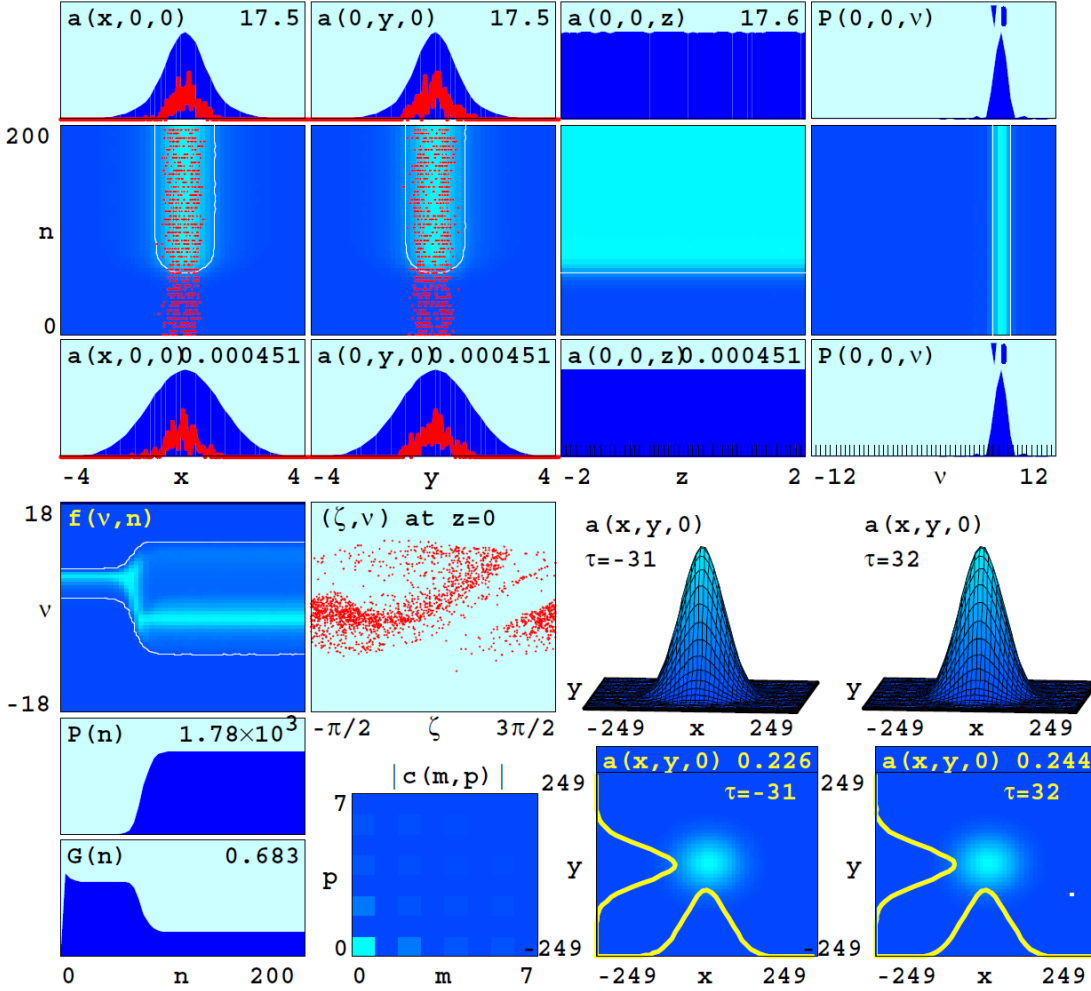


Figure 16. NPS 4-D long pulse multi-pass simulation results for oscillator in the $1.0 \mu\text{m} \rightarrow 1.1 \mu\text{m}$ transmission window

From the inset showing the evolution of optical power as a function of electron phase velocity $P(0,0,v)$ against n (top right), we see that the spectrum peak is not at the resonant wavelength. This presents a challenge in the design of oscillators since this can shift the lasing wavelength beyond the $1.0 \mu\text{m} \rightarrow 1.1 \mu\text{m}$ window. To resolve this, the wavelength shift is factored into the subsequent design iterations such that lasing within

the $1.0 \mu\text{m} \rightarrow 1.1 \mu\text{m}$ window is achieved. From the inset showing the evolution of phase velocity distribution $f(v, n)$ (middle left), we see most of the electrons start out well above resonance at $v_0 \approx 6$ and end up trapped inside the separatrix near resonance at $v_0 \approx 0$ after $n \approx 80$ passes. In addition, from the inset showing the phase space plot of the electrons after $n \approx 200$ passes (middle left), we can also see a majority of the electrons bunched near resonance. Both of these indicate that most electrons have lost energy to the optical beam (recall that $\Delta v = 4\pi N \frac{\Delta\gamma}{\gamma}$). From the inset showing the evolution of power and gain against n (bottom left), we see that both power and gain have saturated by $n \approx 80$ passes. The power and gain remain constant up until $n = 200$ passes, indicating that the oscillator power and gain have stabilized. The inset showing the Hermite-Gaussian modes indicates good beam quality with most of the optical beam in the fundamental mode.

The characteristics of the modeled oscillator are given in Table 13. A lasing linewidth of 14.7 nm at a lasing wavelength of 1073 nm allows us to stay within the transmission window of $1.0 \mu\text{m} \rightarrow 1.1 \mu\text{m}$. An extraction of 2.08% allows us to achieve an average optical beam power of 1.04 MW, which exceeds our target of 1 MW.

Table 13. Oscillator characteristics for $1.0 \mu\text{m} \rightarrow 1.1 \mu\text{m}$ transmission window

Parameter	Value
Extraction	2.08%
Resonant wavelength	1.010 μm
Lasing wavelength	1.073 μm
Lasing Linewidth (full width half maximum)	14.7 nm
Average Optical Beam Power	1.04 MW

3. FEL Amplifier for $1.6 \mu\text{m} \rightarrow 1.7 \mu\text{m}$ Transmission Window

The simulation results of the amplifier for the $1.6 \mu\text{m} \rightarrow 1.7 \mu\text{m}$ transmission window are shown in Figure 17.

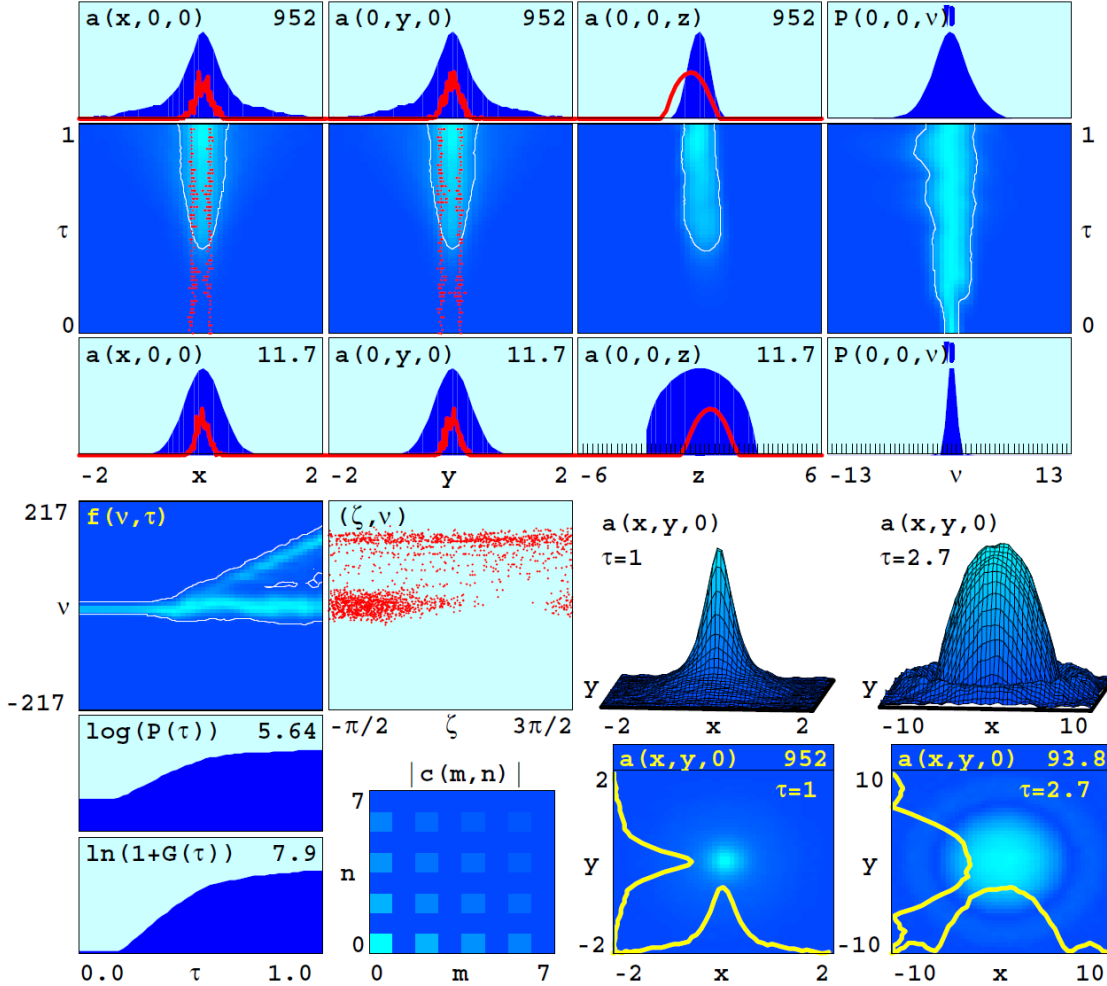


Figure 17. NPS 4-D single pass simulation results for amplifier in the $1.6 \mu\text{m} \rightarrow 1.7 \mu\text{m}$ transmission window

From the insets we can see that similar results are obtained when compared to the $1.0 \mu\text{m} \rightarrow 1.1 \mu\text{m}$ amplifier. The $P(0, 0, v)$ against τ inset (top right) shows widening of the optical spectrum width while the wavelength of the spectrum peak remains unchanged. The $f(v, \tau)$ (middle left) and final phase space (middle center) insets show

the electrons distinctly losing their energy to the optical beam, indicating optimal taper start position and taper rate. The evolution of power and gain (bottom left) show that both power and gain continue to increase beyond the point where taper is started at $\tau = 0.4$, indicating that tapering has been successfully applied to delay saturation. Similarly, the inset showing the Hermite-Gaussian modes indicates poor beam quality with multiple non-fundamental modes present.

The characteristics of the modeled amplifier are given in Table 14. The amplifier lases at $1.550 \mu\text{m}$, which is the closest match to the transmission window of $1.6 \mu\text{m} \rightarrow 1.7 \mu\text{m}$ given the constraints of seed laser availability. An extraction of 3.07% allows us to achieve an average optical beam power of 1.228 MW, which exceeds our target of 1 MW.

Table 14. Amplifier characteristics for $1.6 \mu\text{m} \rightarrow 1.7 \mu\text{m}$ transmission window

Parameter	Value
Extraction	3.07%
Lasing wavelength	$1.550 \mu\text{m}$
Lasing Linewidth (full width half maximum)	5.2 nm
Average Optical Beam Power	1.228 MW

4. FEL Oscillator for $1.6 \mu\text{m} \rightarrow 1.7 \mu\text{m}$ Transmission Window

The simulation results of the oscillator for the $1.6 \mu\text{m} \rightarrow 1.7 \mu\text{m}$ transmission window are shown in Figure 18.

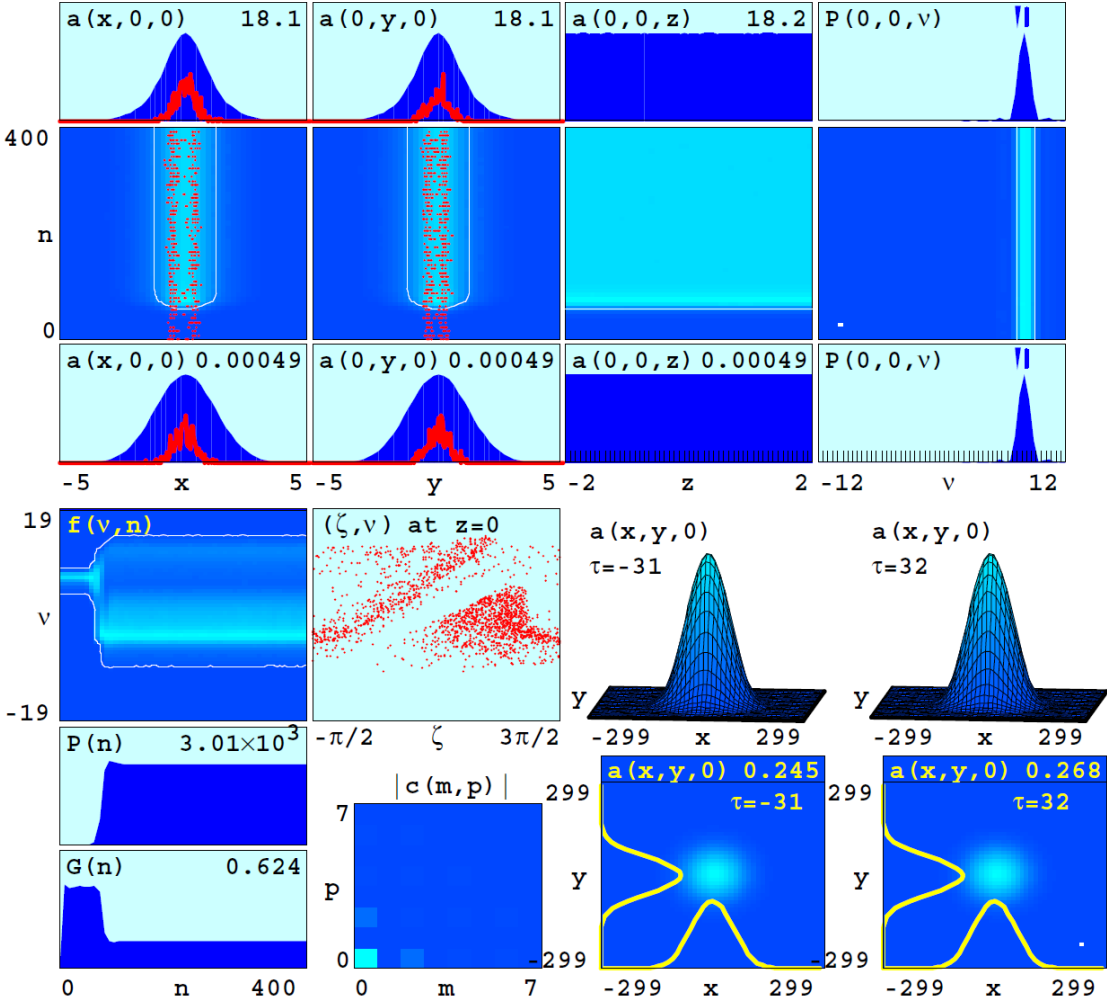


Figure 18. NPS 4-D long pulse multi-pass simulation results for oscillator in the $1.6 \mu\text{m} \rightarrow 1.7 \mu\text{m}$ transmission window

From the insets, we can see that similar results are obtained when compared to the $1.0 \mu\text{m} \rightarrow 1.1 \mu\text{m}$ oscillator. The $P(0,0,v)$ against n inset (top right) shows a significant shift in the wavelength of the optical spectrum peak from the resonant wavelength. The $f(v,n)$ (middle left) and final phase space (middle center) insets show the electrons distinctly losing their energy to the optical beam. The evolution of power and gain show that both power and gain saturate when $n \approx 100$ passes and remain stable thereafter. Similarly, the inset showing the Hermite-Gaussian modes indicates good beam quality with most of the optical beam in the fundamental mode.

The characteristics of the modeled oscillator are given in Table 15. A lasing linewidth of 22.6 nm at a lasing wavelength of 1672 nm allows us to stay within the transmission window of $1.6 \mu\text{m} \rightarrow 1.7 \mu\text{m}$. An extraction of 2.7% allows us to achieve an average optical beam power of 1.08 MW, which exceeds our target of 1 MW.

Table 15. Oscillator characteristics for $1.6 \mu\text{m} \rightarrow 1.7 \mu\text{m}$ transmission window

Parameter	Value
Extraction	2.70%
Resonant wavelength	$1.554 \mu\text{m}$
Lasing wavelength	$1.672 \mu\text{m}$
Lasing Linewidth (full width half maximum)	22.6 nm
Average Optical Beam Power	1.08 MW

THIS PAGE INTENTIONALLY LEFT BLANK

VII. PROPAGATION ANALYSIS OF MEGAWATT CLASS FREE ELECTRON LASERS

With the four FEL designs that we established in the preceding chapter, we now proceed to perform propagation and lethality analysis on them to ascertain their effectiveness in the deployment environment. We determine the extinction coefficients unique to each design's lasing wavelength and specify environmental parameters identical to that given in Table 1 for a tropical maritime environment. In addition, we set the turbulence refractive structure constant C_n^2 at sea level to $10^{-15} \text{ m}^{-\frac{2}{3}}$ to simulate moderate turbulence. The diameter of the beam director aperture is set to 0.3 m, while the platform jitter is given as 5×10^{-6} µrad (root-mean-square value). The wind direction is set perpendicular to beam director azimuth to minimize the effects of thermal blooming. A summary of these parameters is given in Table 16. With specified values of optical beam power and beam quality M^2 , taking into account all the atmospheric attenuation effects as mentioned in Chapter IV, we use ANCHOR to simulate beam propagation through the atmosphere to arrive at the irradiance on target.

Table 16. ANCHOR parameters for propagation analysis

Parameter	Value
Turbulence refractive structure constant C_n^2 (Hufnagel-Valley model)	$10^{-15} \text{ m}^{-\frac{2}{3}}$ (at sea level)
Diameter of beam director aperture	0.3 m
Platform jitter (root-mean-square)	5×10^{-6} µrad
Wind direction	Perpendicular to beam director azimuth
Wind speed (Bufton model)	5 m/s (at sea level)
Extinction coefficients (MODTRAN)	Tropical maritime

A. PERFORMANCE METRICS

We define the target of interest as a sea skimming anti-ship missile. To achieve a hard-kill, we assume that the laser needs to melt a hole of diameter 10 cm through the missile skin that has a thickness of 3 mm [5]. The missile skin material is assumed to be aluminum. To be effective against both sub-sonic and super-sonic missiles, and to be able to engage multiple threats, a dwell time of 2 seconds or less is desired.

Two different performance metrics are used to determine the effectiveness of the FEL designs—the peak irradiance I_p and the required dwell time τ_D . The peak irradiance I_p takes into account effects of diffraction, turbulence, platform jitter, and thermal blooming. Peak irradiance values are independent of the nature of the target.

The required dwell time τ_D can be estimated by

$$\tau_D = \frac{Q_{tot}}{\kappa P_B - P_C - P_R} \quad (45)$$

where Q_{tot} is the total energy required to melt a volume V of aluminum of diameter 10 cm and thickness 3 mm, κ is the fraction of optical power absorbed by the aluminum, P_B is the power-in-the-bucket, and P_C and P_R are the power loss through conductive and radiative means, respectively. For aluminum, $\kappa \approx 0.2$ for infrared wavelengths. The power-in-the-bucket P_B is the total power that falls within the bucket radius, defined here as $r_b = 5$ cm.

B. PROPAGATION MODELING RESULTS

We now proceed to examine the impact that lasing wavelength, beam quality and beam power have on the two performance metrics we have described.

1. Wavelength Sensitivity Analysis

We start by examining the FEL's effectiveness across the lasing wavelengths attained in the amplifier and oscillator FEL designs in Chapter VI. We assume a beam quality of $M^2 = 1$ and beam power of $P = 1$ MW across the lasing wavelengths of

1064 nm, 1073 nm, 1550 nm, and 1672 nm. The plots of the peak irradiance I_p achieved on target and the required dwell times τ_D across a vertical section in the engagement volume are given in Figure 19 and Figure 20, respectively. The horizontal axis shows the horizontal range to the target, while the vertical axis shows the target's altitude. The peak irradiance I_p achieved on target varies from 1 MW/m² (blue on the color scale) to 1000 MW/m² (red on the color scale). From left to right, the three contour lines indicate I_p values of 20 MW/m², 10 MW/m², and 5 MW/m², respectively.

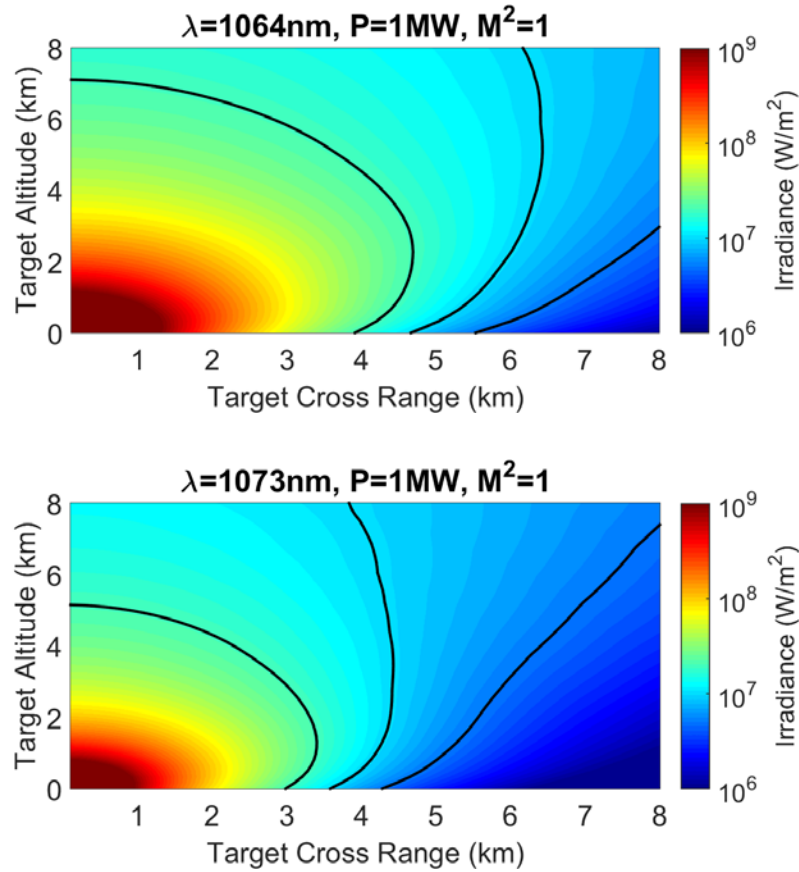


Figure 19. Peak irradiance I_p achieved on target vs. target range and altitude across lasing wavelengths $\lambda = 1064$ nm, 1073 nm, 1550 nm and 1672 nm.

From left to right, the black contour lines indicate I_p values of 20 MW/m², 10 MW/m² and 5 MW/m², respectively.
(Continued on next page.)

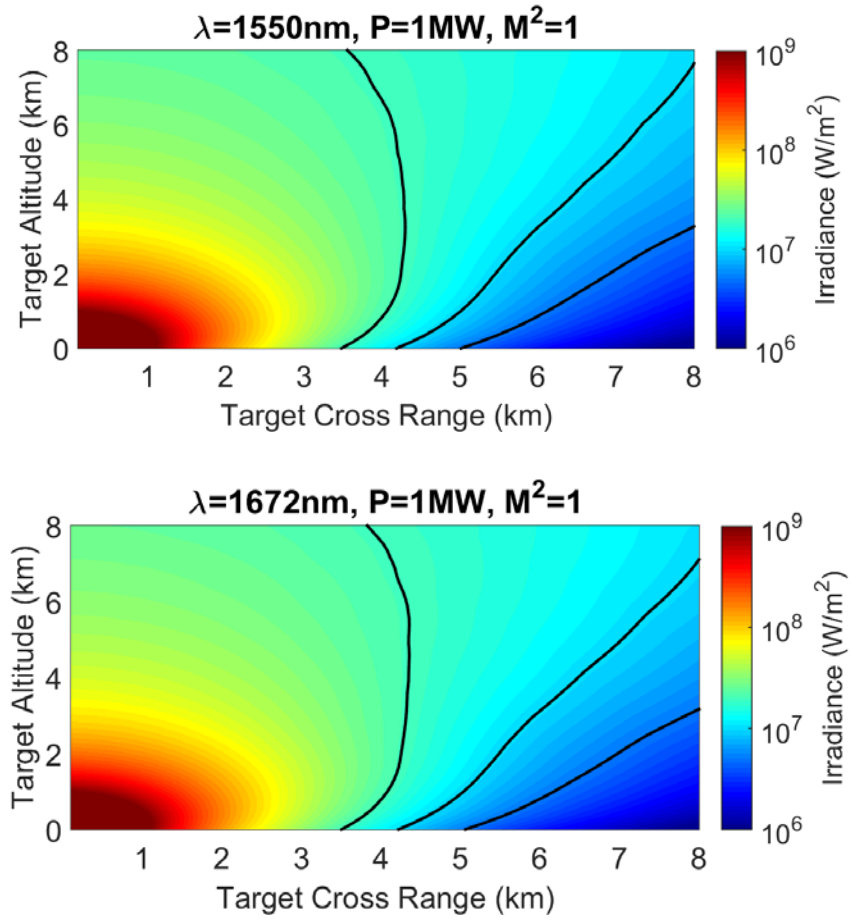


Figure 19. Continued from previous page.

From Figure 19, we can see that at low altitudes, a given I_p value occurs at similar ranges for the lasing wavelengths of 1550 nm and 1672 nm, with the lasing wavelength of 1064 nm achieving the same I_p value at ranges ~ 0.5 km beyond the other two wavelengths. However, for higher altitudes, the same I_p value occurs at a greater range for the lasing wavelengths of 1550 nm and 1672 nm. This trend is a result of the atmospheric extinction profiles at these wavelengths. While the total extinction coefficients for the wavelengths of 1064 nm, 1550 nm, and 1672 nm remain similar at low altitudes, at higher altitudes, according to MODTRAN, the total extinction coefficients for the wavelengths of 1550 nm and 1672 nm decrease more rapidly than that

for the wavelength of 1064 nm, hence resulting in reduced attenuation of the peak irradiance on target I_p .

While the lasing wavelength of 1073 nm fell within our transmission window of $1.0 \mu\text{m} \rightarrow 1.1 \mu\text{m}$, we see a marked decrease in I_p values at a given range compared to the other three wavelengths. We find that the atmospheric extinction coefficients for absorption at the wavelength of 1073 nm are larger than those for all the other three wavelengths, hence resulting in greater attenuation of the peak irradiance on target I_p .

The ANCHOR simulations here only take into consideration a single specified lasing wavelength with a narrow linewidth. From Chapter VI, we know that all of our FEL designs have lasing linewidths ranging from 3.5 nm to 22.6 nm. As the atmospheric extinction coefficients can vary significantly on the sub-nanometer wavelength scale, a more accurate analysis could be done by incorporating the effects of a finite linewidth.

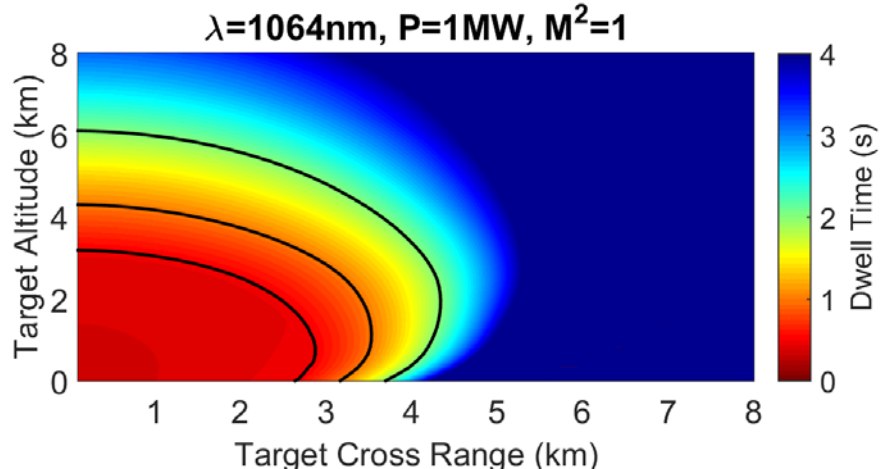


Figure 20. Required dwell times to melt the target τ_D vs. target range and altitude across lasing wavelengths $\lambda = 1064 \text{ nm}, 1073 \text{ nm}, 1550 \text{ nm},$ and 1672 nm . From left to right, the black contour lines indicate required dwell times of $\tau_D = 0.5 \text{ s}, 1 \text{ s}$ and 2 s , respectively.

(Continued on next page.)

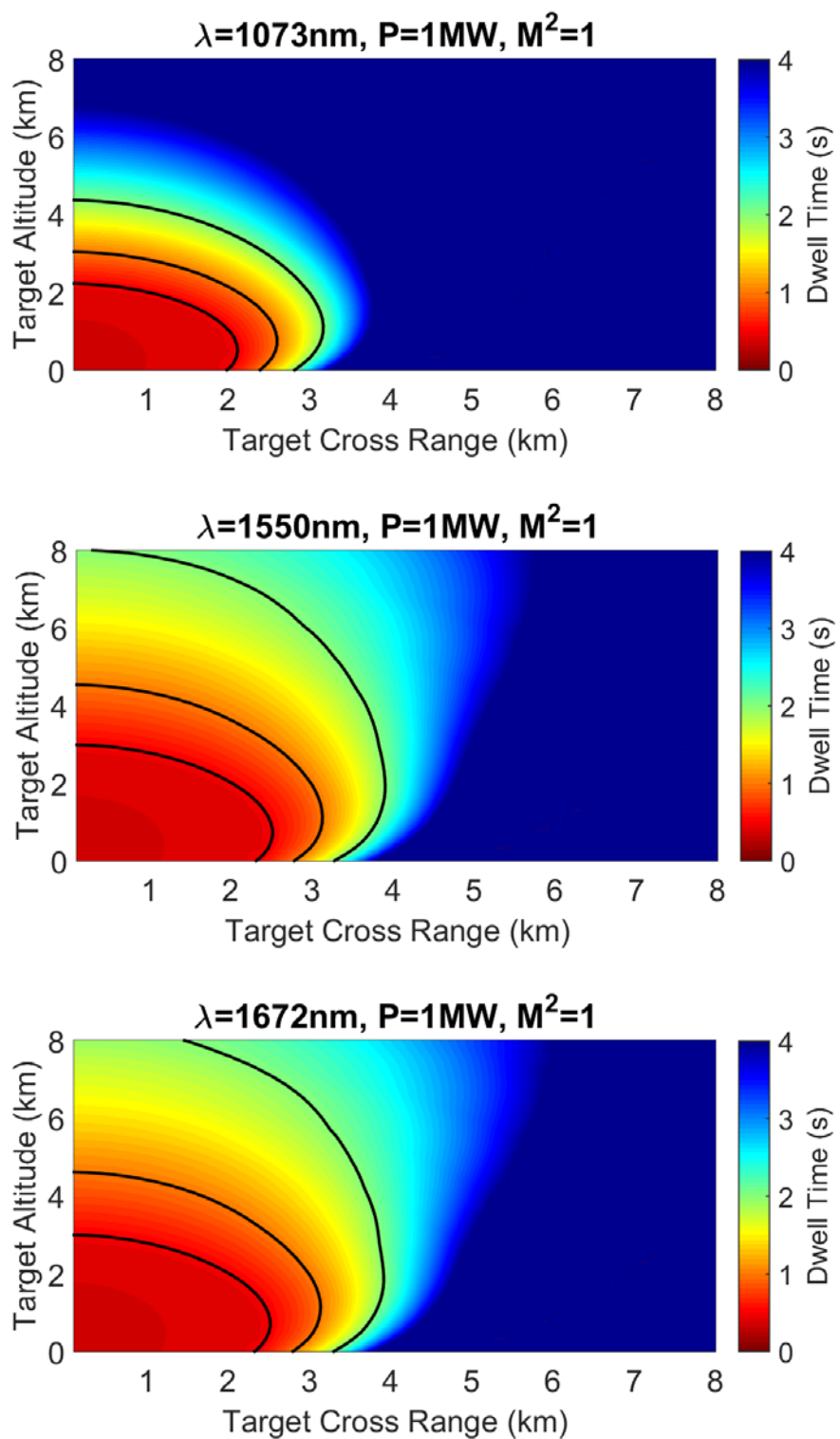


Figure 20. Continued from previous page.

From Figure 20, the contour lines for the required dwell times τ_D of 0.5 s, 1 s, and 2 s show the same trend as the I_p contour lines in Figure 19. For low altitude, the range to melt the target for a given dwell time τ_D is fairly similar for the lasing wavelengths of 1550 nm and 1672 nm; at the wavelength of 1064 nm, the range to melt the target is several hundreds of meters further out than the other two wavelengths. However, for the same dwell time, the range is further for the longer wavelengths of 1550 nm and 1672 nm at higher altitudes. Similarly, at the wavelength of 1073 nm, the range to melt the target for a given dwell time is much less than for the other three wavelengths.

2. Beam Quality Sensitivity Analysis

Next, we move on to explore the impact of the optical beam quality M^2 on the FEL's effectiveness. Using a beam power of $P = 1$ MW and a lasing wavelength of 1064 nm, we plot the peak irradiance achieved on target I_p and the required dwell times τ_D across a vertical section in the engagement volume for the M^2 values of 1, 3, 5, and 7. The plots are given in Figures 21 and 22.

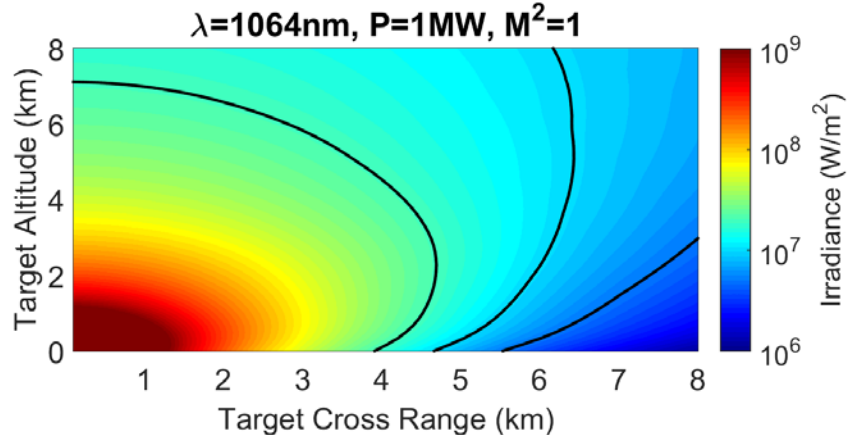


Figure 21. Peak irradiance I_p achieved on target vs. target range and altitude for M^2 values of 1, 3, 5, and 7. From left to right, the black contour lines indicate I_p values of 20 MW/m^2 , 10 MW/m^2 and 5 MW/m^2 , respectively.

(Continued on next page.)

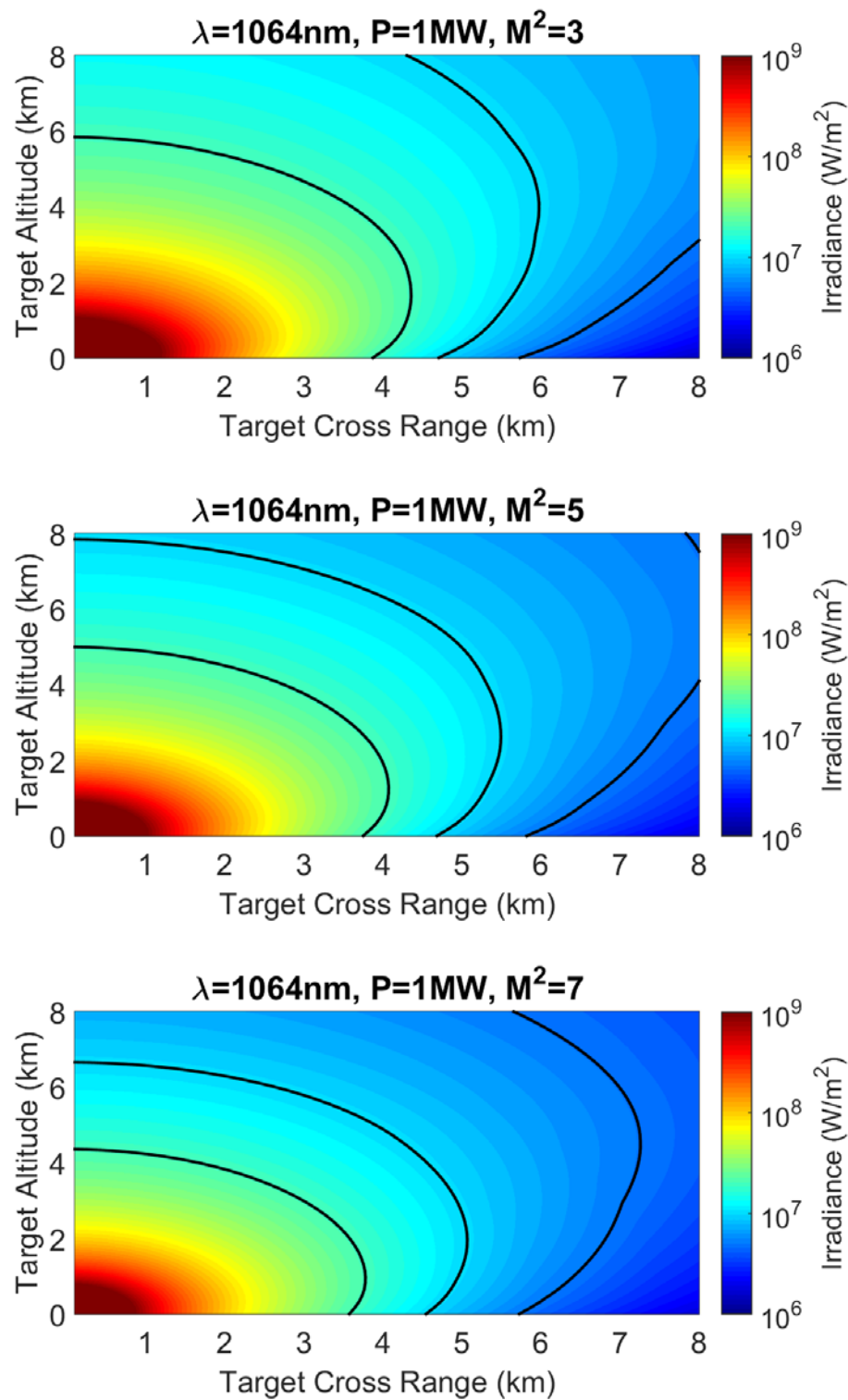


Figure 21. Continued from previous page.

From Figure 21, we can see that at low altitude, the I_p contour lines for the M^2 values of 1, 3, 5, and 7 occur at similar ranges. However, at higher altitudes, the I_p contour lines for $M^2 = 1$ occur at the greatest range, and the contour lines decrease in range as we increase the value of M^2 . We notice that the I_p contour lines in these plots occur at ranges and altitudes in excess of ~ 3.5 km. At these ranges, both turbulence and thermal blooming at low altitudes becomes more severe than turbulence and thermal blooming at high altitudes. Hence, at lower altitudes, the effects of both turbulence and thermal blooming dominate, while at higher altitudes, the effects of beam quality M^2 play a greater role.

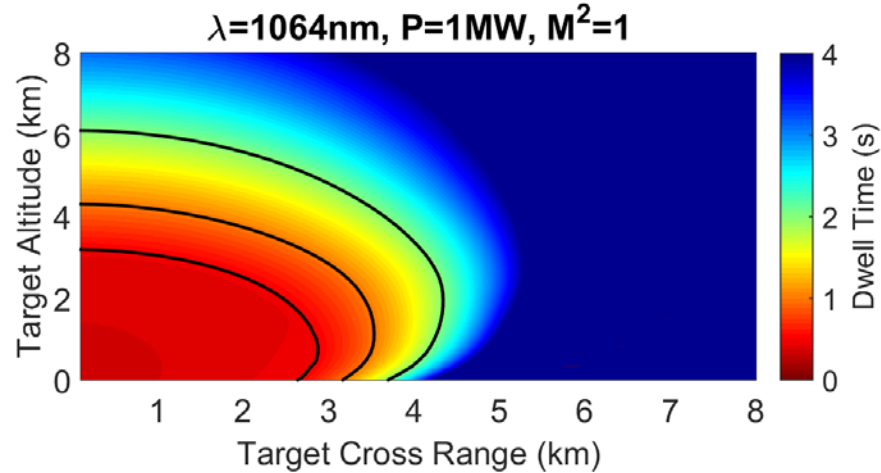


Figure 22. Required dwell times τ_D to melt the target vs. target range and altitude for M^2 values of 1, 3, 5, and 7. From left to right, the black contour lines indicate required dwell times of τ_D of 0.5 s, 1 s, and 2 s, respectively. (Continued to next page.)

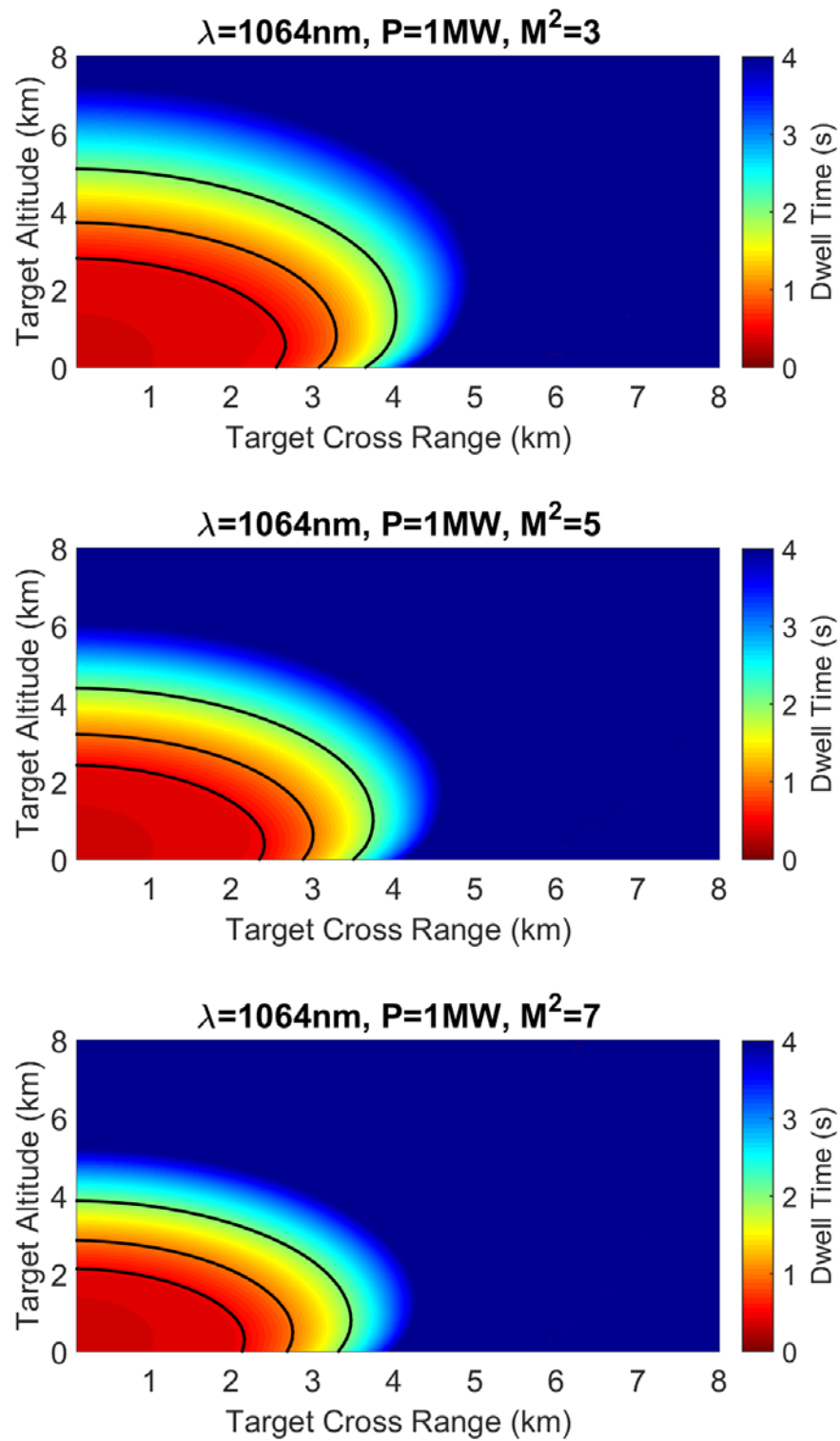


Figure 22. Continued from previous page.

From Figure 22, at high altitudes, the contour lines for required dwell times τ_D of 0.5 s, 1 s, and 2 s show the same trend as the peak irradiance on target I_p contour lines in Figure 21. At high altitudes, the I_p contour lines decrease in range as the value of beam quality M^2 increases. However, at lower altitudes, we also see the I_p contour lines decrease in range slightly as the value of M^2 increases. For lower altitudes, these I_p contour lines occur at ranges of around 2 km to 4 km. At these ranges, the effects of thermal blooming and turbulence are less severe than what we saw in Figure 21 (where I_p contour lines at low altitude occurred at ranges in excess of ~ 3.5 km), hence the effects of the beam quality M^2 on the required dwell times are observed.

3. Beam Power Sensitivity Analysis

Finally, we end with analyzing the impact of optical beam power P on the FEL's effectiveness. We can vary the electron beam pulse repetition frequency to scale the optical beam power accordingly. Using a lasing wavelength of 1064 nm and a beam quality $M^2 = 1$, we plot the peak irradiance achieved on target I_p and the required dwell times τ_D across a vertical section in the engagement volume for a beam power P of 1 MW, 800 kW, 600 kW, and 400 kW. The plots are given in Figures 23 and 24.

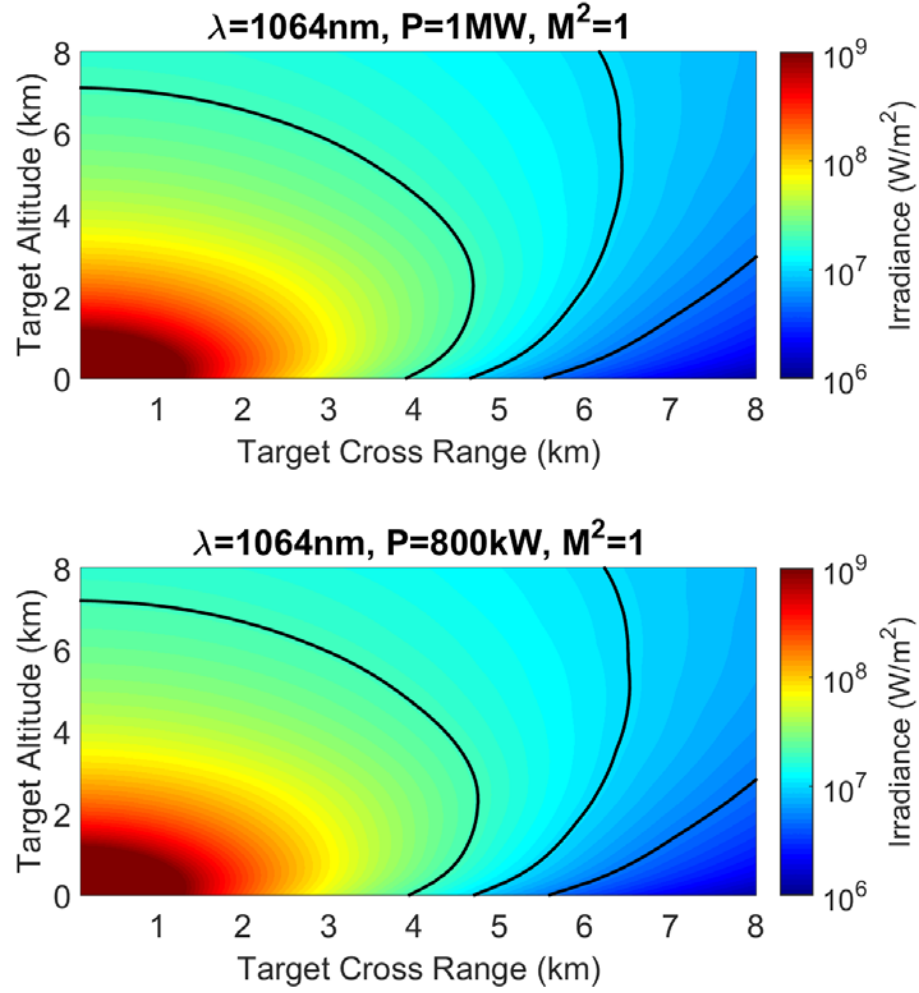


Figure 23. Peak irradiance I_p achieved on target vs. target range and altitude for beam power P of 1 MW, 800 kW, 600 kW, and 400 kW. From left to right, the black contour lines indicate I_p values of 20 MW/m^2 , 10 MW/m^2 , and 5 MW/m^2 , respectively. (Continued on next page.)

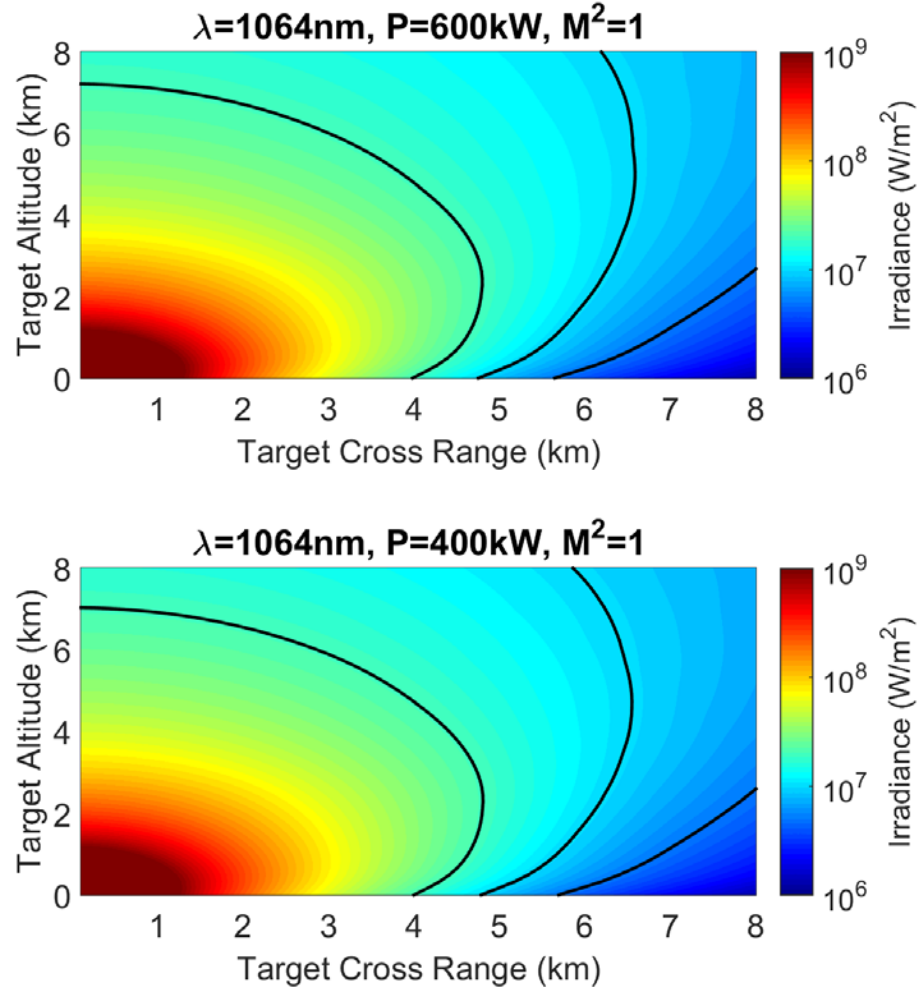


Figure 23. Continued from previous page.

From Figure 23, contrary to what some might expect, a decrease in optical beam power from 1 MW to 400 kW does not lead to any significant decrease in peak irradiance I_p on target. We see this trend clearly at both low and high altitudes. We observe that the I_p contour lines occur at ranges and altitudes in excess of ~ 4 km. At these ranges, the Strehl ratio decreases steadily as the beam power increases, indicating that thermal blooming increases in severity as beam power increases. Hence, the effects of thermal blooming tend to negate the benefits of higher beam power, at least from the perspective of peak irradiance on target.

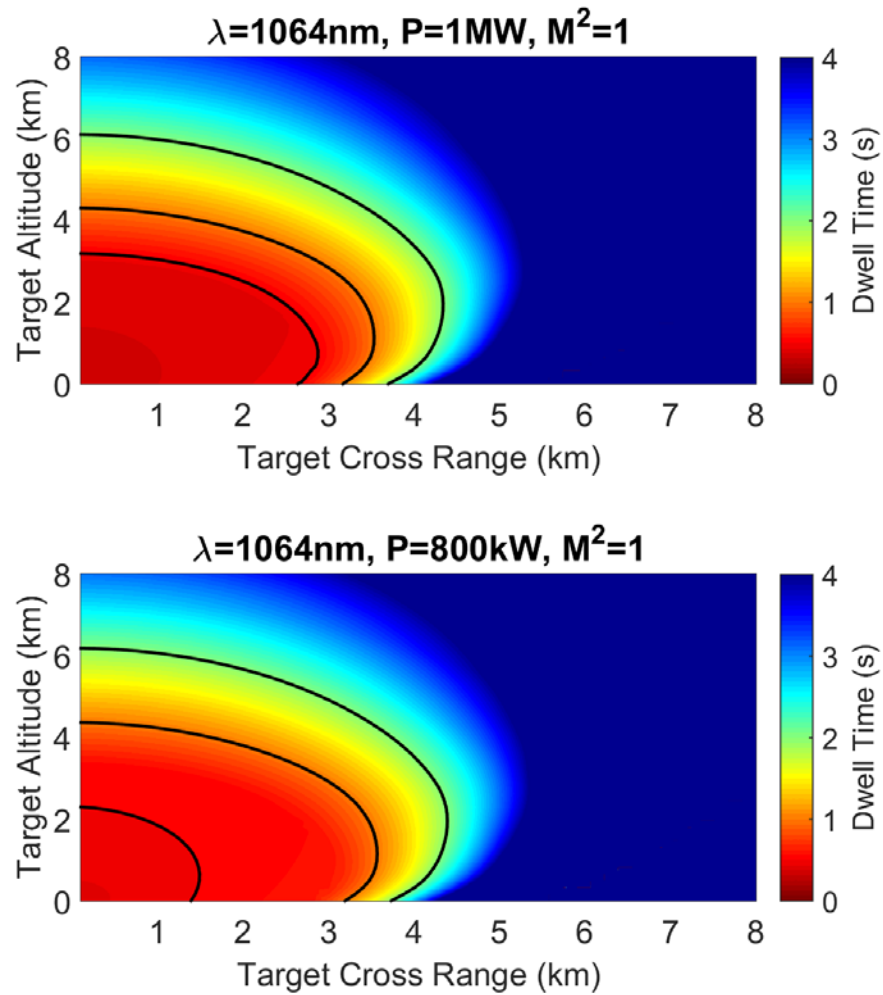


Figure 24. Required dwell times τ_D to melt the target vs. target range and altitude for beam power P of 1 MW, 800 kW, 600 kW, and 400 kW. From left to right, the black contour lines indicate required dwell times of $\tau_D = 0.5$ s, 1 s, and 2 s, respectively. (Continued on next page.)

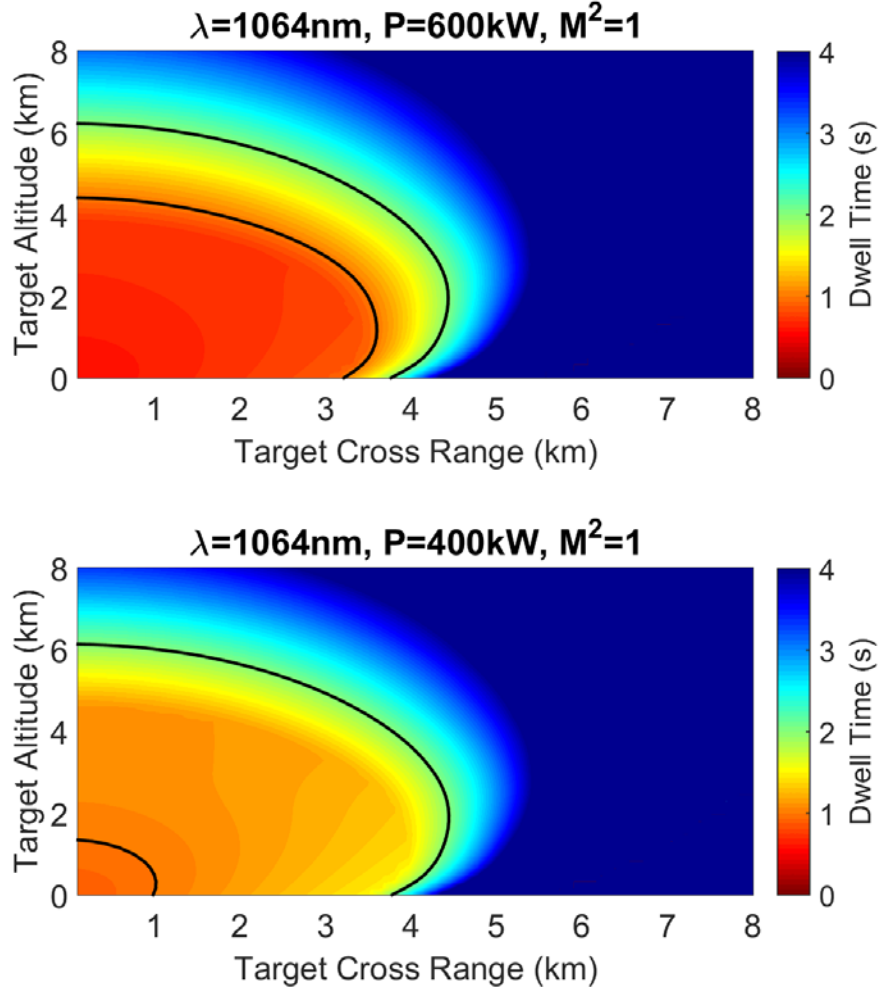


Figure 24. Continued from previous page.

From Figure 24, we can make three observations. First, the contour lines for a required dwell time τ_D of 2 s are very similar across all values of beam power. This indicates that at ranges corresponding to $\tau_D \approx 2$ s, the effects of thermal blooming are such that any increase in beam power beyond 400 kW does not translate to an increase in the power-in-the-bucket P_B . As 2 s is the maximum required dwell time we desire for engagement of both super-sonic and sub-sonic missiles, we can see that the maximum effective range for the selected target is ~ 4 km near the surface, regardless of the beam power.

Second, the contour lines for $\tau_D = 1$ s are also very similar for a beam power P of 1 MW, 800 kW, and 600 kW, again due to the effects of thermal blooming. However, for a beam power P of 400 kW, this contour line decreases substantially. This indicates that while increasing the beam power beyond 600 kW does not result in an increase in the range of the $\tau_D = 1$ contour line, decreasing the beam power to 400 kW results in a significant drop of this range. We can deduce that for a given τ_D contour line, there exists an optimal value of beam power to achieve maximum range. Here, the optimal beam power is ~ 600 kW.

Third, the contour lines for $\tau_D = 0.5$ s fall off quickly from 1 MW to 800 kW and disappear completely from the 600 kW and 400 kW plots. This indicates that the required dwell times of 0.5 s or less are highly sensitive to variations in the beam power. We also note that the contours for $\tau_D = 0.5$ s both occur within a range of ~ 3 km or less. We can deduce that for shorter ranges (~ 3 km or less), the effects of thermal blooming become significantly reduced such that beam power now becomes a primary determining factor for the required dwell time.

Looking across all three observations, we can see several trends at low altitudes. At longer ranges (greater than ~ 4 km), the required dwell time to melt the target becomes independent of beam power due to thermal blooming. There is little advantage in scaling up beam power from 400 kW to 1 MW. However, at shorter ranges (less than ~ 3 km), the required dwell time becomes dependent on beam power. Here, scaling up beam power to 1 MW becomes advantageous. The transition between longer and shorter ranges is dependent on weather conditions (e.g., wind speed and turbulence); nevertheless, the general trends observed here remain valid. Hence, for each engagement range and weather condition, we know that there exists an optimal beam power.

VIII. CONCLUSION

Using various optimization techniques for the amplifier and oscillator configurations, we have successfully designed and simulated FELs with optical beam power output in excess of 1 MW. The effectiveness of these designs against a chosen target of interest in the given deployment environment was established using various performance metrics.

In December 2010, the U.S. Navy assessed FELs as having a technology readiness level of 4 [6]. Additionally, in March 2011, the Navy mentioned in a press report that “[it] is putting [FELs] on the back burner as it focuses on a solid-state laser (SSL) as the quickest way to get a directed-energy weapon to the fleet” [6]. In view of these developments, the push for the technology maturation of FELs for weapon applications has slowed down in the recent decade. While the FEL modeling was performed using parameters that existing FELs have not yet achieved, the results and the analysis remain equally valid notwithstanding the unavailability of FELs with such performance requirements.

Although the propagation analysis we performed in Chapter VII was tailored to our FEL designs attained in Chapter VI, the results are valid for high energy lasers (HELs) in general. Looking across the results attained, we can conclude that the need for FELs is highly dependent on how hard and time-critical our target of interest is. Megawatt class FELs excel in engagement of sub-sonic and super-sonic sea skimming anti-ship missiles where achieving a hard kill in a matter of a couple of seconds is critical. However, for softer and slower moving targets, SSLs with a few hundred kilowatts of beam power would suffice.

Further work could be done with the findings in this thesis. In the area of FEL design and analysis, optimization of the $1.6 \mu\text{m} \rightarrow 1.7 \mu\text{m}$ oscillator optical cavity length could be done to give us a more compact system while still keeping optical intensity at the mirrors to below 200 kW/cm^2 . In the area of propagation analysis, the averaging of

atmospheric extinction coefficients over the linewidth of the laser could be done to give us a more accurate representation of the true atmospheric attenuation.

LIST OF REFERENCES

- [1] T. C. Katsouleas et al., *Scientific Assessment of High-Power Free-Electron Laser Technology*. Washington, DC: National Academies Press, 2009, pp. 7–8.
- [2] J. Blau et al., “High average power free-electron lasers,” *Optical Eng.*, vol. 52, no. 2, pp. 021013-1 – 021013-8, Feb. 2013.
- [3] D. W. Small et al., “Free electron lasers with short Rayleigh length,” *Nucl. Instruments and Methods in Physics Research*, vol. A 393, pp. 262–264, 1997.
- [4] O. Svelto, *Principles of Lasers*, 5th ed. New York, NY: Springer Science, 2010, pp. 153–154.
- [5] S. G. Leonard, “Laser Options for National Missile Defense,” M.S. thesis, Air Command and Staff College, Maxwell Air Force Base, AL, 1998, pp. 47–48.
- [6] R. O’Rourke, “Navy Shipboard Lasers for Surface, Air and Missile Defense: Background and Issues for Congress,” Congressional Research Service, Washington, DC, report number R41526, June 12, 2015, pp. 12–13.

THIS PAGE INTENTIONALLY LEFT BLANK

INITIAL DISTRIBUTION LIST

1. Defense Technical Information Center
Ft. Belvoir, Virginia
2. Dudley Knox Library
Naval Postgraduate School
Monterey, California